International Journal of Mechanical Sciences 309 (2026) 111006

Contents lists available at ScienceDirect

International Journal of Mechanical Sciences

journal homepage: www.elsevier.com/locate/ijmecsci

Extremal micropolar materials for elastic wave cloaking

Dingxin Sun [a], Yi Chen [b,c,*], Xiaoning Liu [a,d], Gengkai Hu [a,*]

[a] School of Aerospace Engineering, Beijing Institute of Technology, Beijing 100081, China
[b] Institute of Nanotechnology, Karlsruhe Institute of Technology, Karlsruhe 76128, Germany
[c] Institute of Applied Physics, Karlsruhe Institute of Technology, Karlsruhe 76128, Germany
[d] School of Civil Engineering, Changsha University of Science & Technology, Changsha 410114, China

ARTICLE INFO

Dataset link: https://dx.doi.org/10.5281/zenodo.17141180

Keywords:
Asymmetric transformation elasticity
Elastic cloak
Micropolar elasticity
Soft modes
Extremal micropolar material
Lattice metamaterials

ABSTRACT

The asymmetric transformation elasticity provides a promising method for controlling elastic waves. However, it requires elastic materials capable of supporting asymmetric stresses, which are not admissible within the linearized Cauchy elasticity under small deformations. In contrast, asymmetric stress tensors naturally arise in micropolar continuum theory, yet the connection between micropolar media and the asymmetric transformation elasticity has remained largely unexplored. In this work, we demonstrate that extremal micropolar media, which are micropolar materials exhibiting soft modes, can be used to design elastic cloaks via asymmetric transformation elasticity. Our first contribution is to establish a rigorous theoretical formulation of the asymmetric transformation method within the micropolar continuum framework. Second, we propose a micropolar metamaterial model that exhibits required soft modes for cloaking. A two-dimensional metamaterial cloak is then constructed and its cloaking performance is verified through full-wave numerical simulations. This study unveils a novel strategy for controlling elastic waves through micropolar media and also sheds light on interesting physical properties of extremal micropolar materials.

1. Introduction

Transformation theory, firstly proposed in electromagnetic wave fields [1], has become a successful design tool for various wave fields, e.g., acoustic waves, optics and so on [2–6]. Many interesting wave devices have been designed based on this theory over the past decade, such as omni-directional absorbers or cloaks [7–9]. However, the application of transformation theory for elastic waves is still challenging due to the complexity of elastic waves, which contain both longitudinal components and transverse components. Transformation elasticity is mainly available for a number of limited situations, e.g., flexure waves in plates or approximation control at high frequency range [10,11].

Controlling elastic waves via transformation elasticity generally requires two steps. Firstly, the Navier equation for Cauchy materials in a virtual space is transformed to a new governing equation in a physical space [2,4]. The second step is to realize materials or metamaterials [12–14] that follow the transformed governing equation. For elastic waves, two types of transformed equations exist. In one case, the transformed equations become quite complex and involve the use of Willis materials [2,15–16], which exhibit coupling between stress/momentum and velocity/strain fields [15]. In recent developments, a formulation of Willis elasticity based on microcontinuum field theory has been proposed, which subsequently enabled the design of elastic cloaks [17]. In another version, the transformed equation has the same form as the Cauchy theory, while the fourth order elasticity tensor loses its minor symmetry, likewise the stress tensor [4,18]. The theory is also called asymmetric transformation elasticity [19]. However, the asymmetric elasticity theory is not physical or well defined, since the theory doesn't not take into the account of the unbalanced angular momentum caused by asymmetric stress. This problem caused concern on the possibility of designing cloaks following the asymmetric transformation elasticity [20]. At first sight, it seems impossible to design an asymmetric elastic material. Interestingly, the propagation of a small disturbance superimposed upon a largely-deformed hyperelastic material (i.e. the small-on-large theory) is governed by an effective asymmetric elasticity tensor [21–23]. Therefore, hyperelastic materials, like semi-linear materials, have been theoretically shown to be able to cloak elastic waves [22–24]. Yet, the cloaking effect is limited due to geometry restrictions [22]. The required hyperelastic behavior is also challenging to achieve with artificial microstructures.

Recently, asymmetric elastic materials have been effectively realized by metamaterials [25–31]. In the first type of design, each unit cell contains a mass block that can freely translate but is restrained against

* Corresponding authors.
E-mail addresses: yi.chen@partner.kit.edu (Y. Chen), hugeng@bit.edu.cn (G. Hu).

https://doi.org/10.1016/j.ijmecsci.2025.111006
Received 10 August 2025; Received in revised form 18 September 2025; Accepted 8 November 2025
Available online 10 November 2025

Nomenclature

$\mathbf{x}$, $\mathbf{X}$	The spatial coordinates in the physical and virtual spaces
F_{ij}, J, η	The mapping gradient tensor, its determinant and the stretching ratio
σ'_{ij}, ε'_{ij}	Transformed stress and strain
C_{0ijkl}, ρ_0	Elasticity tensor and mass density of the background medium
λ_0, μ_0, ν	Lamé constants and Poisson's ratio of the background medium
C'_{ijkl}, ρ'	Transformed elasticity tensor and mass density
ϕ_i, κ_{ij}, m_{ij}	Micro-rotation, curvature and couple stress of micropolar media
C_{ijkl}, ρ	Elasticity tensor and mass density of micropolar media
A_{ijkl}, D_{ijkl}, I	Higher-order elasticity tensor, coupling tensor and micro-rotation inertia
C^{eff}_{ijkl}	Effective asymmetric elasticity tensor of micropolar media
$\boldsymbol{\varepsilon}^{\text{o}}$, $\boldsymbol{\varepsilon}^{\text{d}}$, $\boldsymbol{\varepsilon}^{\text{s}}$, $\boldsymbol{\varepsilon}^{\text{a}}$	Four basic deformation modes of micropolar media with $A_{ijkl} = 0$
$\bar{\varepsilon}, \varepsilon_{\text{d}}, \varepsilon_{\text{s}}, \varepsilon_{\text{a}}$	The projection of the strain onto the four basic modes
$\mathbf{e}_1$, $\mathbf{e}_2$, $\mathbf{e}_r$, $\mathbf{e}_\theta$	Cartesian basis vectors and polar coordinate basis vectors
$\mathbf{a}_i$	Lattice vectors
l, h, d, γ, S_{cell}	Size parameters of the microstructure
k, K, s	Elastic parameters of the microstructure
M, j	Mass and rotational inertia of the mass block
$u_{p,q}$, $v_{p,q}$, $\phi_{p,q}$	Discrete field variables of the discrete metamaterial model
$\mathbf{u}^{\text{I}}_{p,q}$, $\mathbf{u}^{\text{II}}_{p,q}$	Displacements of hidden nodes
m, n	Lattice coordinates relative to (p, q)
$\mathbf{k}$	Wave vector
ω_{r}, ω_{ext}	The optical cut-off angular frequency and the operating angular frequency
c_{T}, c_{L}	Transverse and longitudinal wave velocities of the background medium
N	The number of unit cells per shear wavelength
N_r, N_θ	The number of layers in the cloak along the radial direction and the θ direction
P_ϕ	The proportion of micro-rotation kinetic energy
a, b, δ	Size parameters of the cloak
E_{sc}	The total scattered power
P_{in}	The incident power density

rotation by grounded torsional springs [25,26], or by external magnetic fields [31]. The asymmetric stress is balanced by external torque supplied by the torsional springs or the magnetic fields. By employing a complex mechanism that restricts rotational degrees of freedom (DOFs) while permitting translational motion, this type of metamaterial cloak has been experimentally realized [28]. In the second type of design, a discrete metamaterial with local rotational resonance is adopted [29]. The asymmetric shear stress expressed by a metamaterial unit cell is compensated by its inner rotation inertia. Both strategies have been employed to achieve the asymmetric elasticity tensors required for asymmetric transformation. We note here that although asymmetric elasticity theory and its corresponding materials do not naturally occur [4], they can nevertheless be effectively approximated by appropriately designed metamaterials. This reflects a central idea of metamaterials [14], achieving effective-medium properties that are seemingly unattainable in conventional materials, e.g., negative index [32,33]. In this work, we pursue a different route to achieve elastic wave cloaking—through the use of micropolar elastic media, which inherently support asymmetric stress. The advantage lies in the fact that micropolar elasticity is a physically consistent theory with a well-established theoretical foundation, in contrast to the asymmetric elasticity theory. Our initial idea is inspired by the observation that pentamode materials [34–41] can control acoustic waves through the framework of transformation acoustics [42,43]. Pentamode materials are a typical example of extremal Cauchy materials, which allow soft modes that, in principle, incur no strain energy [44–49]. Therefore, we anticipate that special extremal higher-order elastic media [50] can potentially be used to control elastic waves in Cauchy materials. A promising candidate is the micropolar continuum media, also called Cosserat media [51–53], which is relatively simple in mathematics and more importantly can capture asymmetric stresses. We remark that micropolar elasticity was utilized to account for asymmetric stress behavior in granular mechanics [54,55], long before the emergence of transformation theory and metamaterials. Later, the study of surface waves in micropolar media was applied to seismology [56,57]. Recently, some studies have further incorporated micropolar theory into phase-field models to investigate fracture problems [58,59].

In our paper, we particularly focus on the micropolar media with a vanishing higher-order elasticity tensor, also referred to as reduced Cosserat media [60,61], in which all gradients of micro-rotations act as soft modes. We find that a type of extremal micropolar medium, which supports not only these soft modes but also shear–rotation coupled soft modes, can serve as a viable foundation for realizing asymmetric transformation elasticity. Accordingly, we develop design guidelines to achieve the required soft modes and propose a discrete metamaterial that realizes the corresponding extremal micropolar parameters. Furthermore, we design a 2D elastic cloak based on the proposed metamaterial, and demonstrate the effectiveness of both the theory and the metamaterial through numerical simulations.

In contrast to grounded elastic cloaks [25,26,28], the proposed design based on extremal micropolar media eliminates complicate rotational constraints, enabling much simpler design for applications. Compared with our previous elastic cloak based on rotational resonance [29], the current design is not limited to a background medium with a Poisson's ratio below 0.25. Other studies bypass asymmetric elasticity altogether. One common strategy symmetrizes the elasticity tensor for easier implementation, but at the cost of reduced cloaking efficiency [62,63]. Another approach optimizes material parameters or topology for static cloaking, which requires the cloak to be tailored to specific loads [64–66].

Micropolar homogenization has been increasingly developed and applied in recent years to describe biological materials [67], composite materials [68,69], and both two-dimensional (2D) [70–72] and three-dimensional (3D) [73,74] lattice materials. Classical homogenization methods generally determine effective micropolar parameters by establishing energy equivalence between the microstructure and the effective continuum [70,74]. In contrast, this work applies Taylor expansions of the field variables in the dynamic equations, leading to a continuum version of Lagrangian equations. Effective micropolar parameters can then be derived by comparing the coefficients in the governing equations [75]. In recent years, enhanced homogenization methods have been developed to account for nonlocal effects, allowing for improved accuracy in modeling microstructure systems even when the long-wavelength assumption does not hold [76–79]. In designing the metamaterial cloak in this paper, the homogenized material parameters in Cartesian coordinates are adopted. Such an approach remains valid when the metamaterial unit cells are small enough compared to the cloak since the curvature effect on each unit cell is negligible. Existing methods have demonstrated that conformal mapping can be used to directly transform periodic microstructures into quasi-periodic microstructures in polar coordinates, while establishing the relationship between the elasticity tensors before and after mapping [80–82].

Extending such techniques to micropolar framework may improve the accuracy of the cloak design.

The paper is organized as follows. We establish in detail the connection between micropolar continuum theory and asymmetric transformation in Section 2. The required soft modes of extremal micropolar media for transformation are discussed in Section 3. Then, an extremal metamaterial model with required soft modes is proposed and its effective micropolar elastic parameters are derived analytically. We numerically calculate its band structure and simulate its wave behavior to verify the metamaterial design. In Section 4, we design a 2D elastic cloak based on the proposed micropolar metamaterial. The cloaking performance is validated numerically and compared with results from effective-medium model. These results serve to validate our cloaking theory based on extremal micropolar materials. Finally comes the conclusion.

2. Micropolar continuum theory for elastic cloaking

Conventional micropolar media cannot be directly applied for elastic cloaking in Cauchy media, since the number of hard modes in a typical micropolar medium does not match that of a Cauchy medium. The most intuitive manifestation of this mismatch lies in the couple stresses present in micropolar media, which cannot exist in Cauchy elasticity. However, by introducing soft modes and retaining only those hard modes that are compatible with the Cauchy medium, asymmetric transformation elasticity becomes feasible.

In this section, we first briefly review the governing equations of asymmetric elasticity and micropolar elasticity in the 2D case. Then, by imposing the condition $A_{ijkl} = 0$, which corresponds to the presence of two soft modes, we eliminate the micro-rotation ϕ from the linear momentum equations of micropolar elasticity. This yields a governing equation that is formally consistent with that of asymmetric elasticity. By comparing the resulting effective elasticity tensor with the asymmetric elasticity tensor, we identify the required micropolar parameters for implementing asymmetric transformation elasticity.

2.1. Asymmetric transformation elasticity

We briefly revisit the asymmetric transformation elasticity [4] through the example of a 2D annular cloak. A more detailed discussion on the cloak design and material realization will be provided in Section 4. A virtual space (Fig. 1(a)) is assumed to be filled with a Cauchy material with the mass density ρ_0 and the elasticity tensor $C_{0ijkl} = C_{0jikl} = C_{0klij}$. We limit the study in this paper to small deformations and only consider linear elastic waves propagating inside the material. Omitting a time harmonic term $\exp(-\mathrm{i}\omega t)$, with i being the imaginary unit, ω the angular frequency and t the time, the dynamic equation and constitutive equation for waves propagating in the virtual space in frequency domain write as

$$-\rho_0\omega^2 u_i(\mathbf{X}) = \frac{\partial \sigma_{ji}(\mathbf{X})}{\partial X_j},\ \sigma_{ij} = C_{0ijkl}\frac{\partial u_l(\mathbf{X})}{\partial X_k}, \tag{1}$$

in which, $u_i(\mathbf{X})$ and $\sigma_{ij}(\mathbf{X}) = \sigma_{ji}(\mathbf{X})$ represent the displacement and the symmetric stress tensor in the virtual space, respectively.

We consider a spatial mapping $\mathbf{x} = \mathbf{x}(\mathbf{X})$ that maps a circular domain Ω with a small hole in the virtual space onto an annular cloak region Σ in the physical space. The small hole is deliberately introduced in order to obtain a compatible singular-free mapping between the two regions. Otherwise, the required material parameters close to the inner boundary of the cloak will approach zero or infinite. Eq. (1) then can be rewritten as the following form by a change of variable [83]

$$-\rho'\omega^2 u_i'(\mathbf{x}) = \frac{\partial \sigma_{ji}'(\mathbf{x})}{\partial x_j},\ \sigma_{ji}'(\mathbf{x}) = C_{ijkl}'(\mathbf{x})\frac{\partial u_i'(\mathbf{x})}{\partial x_k}. \tag{2}$$

The displacement and stress in the physical space are $u_i'(\mathbf{x}) = u_i(\mathbf{X})$ and $\sigma_{ij}'(\mathbf{x}) = J^{-1}F_{ik}\sigma_{kj}(\mathbf{X})$, respectively. In the formula, the mapping gradient $F_{ij} = \partial x_i/\partial X_j$ and $J = \det(F_{ij})$ are defined. We remark that the mapping gradient $\mathbf{F}$ should not be confused with the deformation gradient in finite deformation elasticity. Here, $\mathbf{F}$ doesn't represent physical deformation but stands for spatial mapping. The mass density and elasticity tensor in the cloak region Σ are

$$\rho'(\mathbf{x}) = J^{-1}\rho_0(\mathbf{X}),\ C_{ijkl}'(\mathbf{x}) = J^{-1}F_{im}F_{kn}C_{0mjnl}(\mathbf{X}). \tag{3}$$

The transformed elasticity tensor maintains the major symmetry $C'_{ijkl} = C'_{klij}$, while violates the minor symmetry $C'_{ijkl} \neq C'_{jikl}$. As a consequence, the transformed stress tensor is not symmetric $\sigma'_{ij} \neq \sigma'_{ji}$. In the above process, the circular domain Ω with a small hole is not physically deformed into the annular region Σ. Instead, the entire process is a purely mathematical mapping or a change of variables. If one assigns materials to the cloak region Σ according to the above parameters in Eq. (3), elastic waves coming from the background domain Σ^{out} cannot detect the cloaked inner region Σ^{in}. For clarity, we assume that the mapping gradient can be diagonalized, i.e., $\mathbf{F} = F_{11}\mathbf{e}_1\otimes\mathbf{e}_1 + F_{22}\mathbf{e}_2\otimes\mathbf{e}_2$, where $\mathbf{e}_1$ and $\mathbf{e}_2$ are the orthonormal basis vectors of the principal coordinate. The material in the virtual space has an isotropic elasticity tensor $C_{0ijkl} = \lambda_0\delta_{ij}\delta_{kl} + \mu_0(\delta_{ik}\delta_{jl} + \delta_{il}\delta_{jk})$. The assumption is valid for mapping for typical wave controlling function, such as cloaks. The required mass density and the elasticity matrix in Eq. (3) for the annular cloak can be simplified in the principal coordinate as

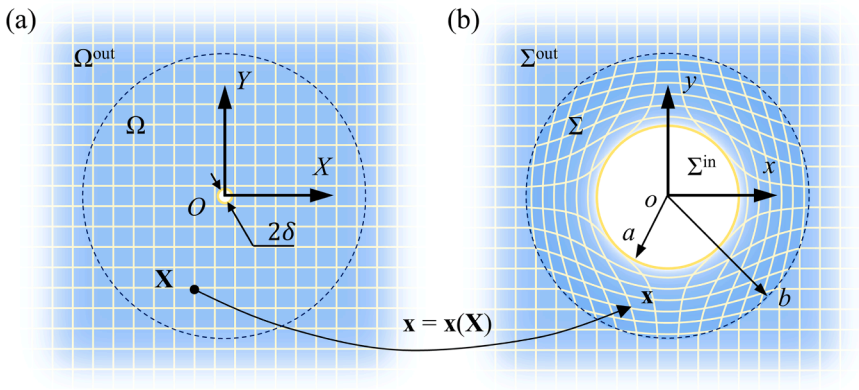

Fig. 1. Illustration of asymmetric transformation elasticity through the design of a 2D cloak. (a) Virtual space with a background domain Ω^{out} and a circular domain Ω with a small hole of 2δ in diameter. (b) Physical space with a background domain Σ^{out}, an annular cloak domain Σ, and a cloaked inner domain Σ^{in}. Cartesian coordinate systems *XOY* and *xoy* are assigned for the virtual space and physical space, respectively. The cloak region Σ in the physical space is mapped from the domain Ω in the virtual space through a spatial mapping $\mathbf{x} = \mathbf{x}(\mathbf{X})$.

$$\rho^{'} = \frac{\rho_0}{F_{11}F_{22}}, \begin{pmatrix} \sigma^{'}_{11} \\ \sigma^{'}_{22} \\ \sigma^{'}_{12} \\ \sigma^{'}_{21} \end{pmatrix} = \begin{pmatrix} C^{'}_{11} & C^{'}_{12} & 0 & 0 \\ C^{'}_{12} & C^{'}_{22} & 0 & 0 \\ 0 & 0 & C^{'}_{66} & C^{'}_{69} \\ 0 & 0 & C^{'}_{69} & C^{'}_{99} \end{pmatrix} \begin{pmatrix} \varepsilon^{'}_{11} \\ \varepsilon^{'}_{22} \\ \varepsilon^{'}_{12} \\ \varepsilon^{'}_{21} \end{pmatrix}, \tag{4}$$

$$\begin{cases} C^{'}_{11} = \eta(\lambda_0 + 2\mu_0), & C^{'}_{22} = \dfrac{\lambda_0 + 2\mu_0}{\eta}, & C^{'}_{12} = \lambda_0, \\ C^{'}_{66} = \eta\mu_0, & C^{'}_{99} = \dfrac{\mu_0}{\eta}, & C^{'}_{69} = \mu_0. \end{cases} \tag{5}$$

Here, the stretching ratio $\eta = F_{11}/F_{22}$ and the asymmetric strain $\varepsilon^{'}_{ij} = u^{'}_{j,i}$ are defined. For a trivial stretching ratio $\eta = 1$, the required material is a conventional Cauchy material with $C^{'}_{66} = C^{'}_{99} = C^{'}_{69} = \mu_0$. For this Cauchy material, an antisymmetric strain or an infinitesimal rotation ($u_{1,1} = u_{2,2} = 0$, $u_{1,2} = -u_{2,1}$) results in zero stresses and can be regarded as its soft mode. However, for a nontrivial ratio $\eta \neq 1$, the required material is an asymmetric elastic material, since the three shear modulus, $C^{'}_{66}$, $C^{'}_{99}$, and $C^{'}_{69}$, are different, which means an infinitesimal rotation can lead to non-zero stresses in the material. It can be verified that the asymmetric material also exhibits an soft mode [25]. This soft mode is a combination of an infinitesimal rotation and a shear deformation, as indicated by $C^{'}_{66}C^{'}_{99} - C^{'2}_{69} = 0$ from Eq. (5). In the following, we will show how to achieve the asymmetric elastic properties using extremal micropolar materials with special soft modes.

2.2. Basics of micropolar continuum theory

We provide a brief introduction to micropolar continuum theory. In micropolar elasticity, micro-rotation DOFs, ϕ_i, in addition to displacement DOFs, u_i, are introduced for each material point. The deformation is characterized by [51]

$$\varepsilon_{ij} = \frac{\partial u_j}{\partial x_i} - \epsilon_{ijk}\phi_k, \ \kappa_{ij} = \frac{\partial \phi_j}{\partial x_i}, \tag{6}$$

where ϵ_{ijk},ε_{ij}, and κ_{ij} represents the Levi-Civita tensor, the micropolar strain tensor and the micropolar curvature tensor, respectively. All indices range from 1 to 2 for 2D space and from 1 to 3 for 3D space. The balance law for linear momentum and angular momentum in frequency domain read

$$-\omega^2\rho u_i = \frac{\partial \sigma_{ji}}{\partial x_j}, -\omega^2 I\phi_i = \frac{\partial m_{ji}}{\partial x_j} + \epsilon_{ijk}\sigma_{jk}, \tag{7}$$

in which, ρ is the mass density, I represents the micro-rotation inertia density (micro-rotation inertia per unit volume), σ_{ij} and m_{ij} stand for the stress tensor and the couple stress tensor, respectively. In Cauchy theory, the stress tensor can be proved to be symmetric from the balance law for angular momentum, owing to the absence of couple stress and micro-rotation DOFs. Here, the micropolar stress doesn't need to be symmetric and the asymmetric part is balanced by the couple stress and the micro-rotation inertia.

For infinitesimal deformations, a quadratic strain energy density function in terms of the micropolar strain and the micropolar curvature is assumed [51]

$$w = \frac{1}{2}\varepsilon_{ij}C_{ijkl}\varepsilon_{kl} + \varepsilon_{ij}D_{ijkl}\kappa_{kl} + \frac{1}{2}\kappa_{ij}A_{ijkl}\kappa_{kl}. \tag{8}$$

The constitutive law for the stress tensor and the couple stress tensor are derived by differentiating the strain energy density w with respect to the strain and the curvature, respectively,

$$\sigma_{ij} = C_{ijkl}\varepsilon_{kl} + D_{ijkl}\kappa_{kl}, \ m_{ij} = D_{klij}\varepsilon_{kl} + A_{ijkl}\kappa_{kl}. \tag{9}$$

The fourth-rank tensor A_{ijkl} is denoted as the higher-order elasticity tensor in micropolar elasticity [74,84] since it accounts for the gradient of micro-rotation — a higher-order deformation measure beyond strain. The micropolar elasticity tensor C_{ijkl} and the higher-order elasticity tensor A_{ijkl} exhibit major symmetry, $C_{ijkl} = C_{klij}$, $A_{ijkl} = A_{klij}$, but not minor symmetry. Both C_{ijkl} and A_{ijkl} are normal tensors, while the coupling tensor D_{ijkl} is a pseudo-tensor [75]. This tensor becomes zero for a material or metamaterial with centrosymmetry [85,86]. In 3D cases, a non-zero coupling tensor enables modeling interesting chiral effects, such as push-to-twisting coupling effect, or circularly polarized transverse elastic waves [87,88]. This paper is concerned with 2D settings. The coupling tensor and higher-order tensor reduce to third-order D_{ijk3} and second-order A_{i3j3}, respectively. The relationship between chirality and centrosymmetry becomes subtle. In particular, a 2D material can still be chiral even with centrosymmetry, such as tetra-chiral or hexa-chiral metamaterials, albeit the coupling tensor becomes zero [52,75,89]. In these cases, chiral effects, e.g., coupling between dilation and rotation, are modeled by certain components of the tensor C_{ijkl} [90,91].

2.3. Micropolar continuum parameters for elasticity cloak

Now, we introduce the similarity between extremal micropolar elastic materials and asymmetric elastic materials, following a previous method [92]. We consider micropolar materials with a zero higher-order elasticity tensor $A_{ijkl} = 0$. Such materials are also called reduced Cosserat media [61]. The zero higher-order tensor leads to soft modes related to the micropolar curvatures. According to thermodynamic stability, the coupling tensor also vanishes $D_{ijkl} = 0$. Both conditions can be met with a proposed micropolar metamaterial later. The constitutive equations and the dynamic equations in Eq. (7) and (9) reduce to

$$\sigma_{ij} = C_{ijkl}\frac{\partial u_l}{\partial x_k} - C_{ijkl}\epsilon_{klm}\phi_m, \ m_{ij} = 0, \tag{10}$$

$$-\omega^2\rho u_i = \frac{\partial \sigma_{ji}}{\partial x_j}, \ -\omega^2 I\phi_i = \epsilon_{ijk}\sigma_{jk}. \tag{11}$$

The displacement DOFs and the micro-rotation DOFs are coupled in the constitutive law. To achieve Eq. (2) for the asymmetric elasticity theory, we need to decouple the displacement and the micro-rotation. Substituting the stress tensor in Eq. (10) into the balance law of angular momentum in Eq. (11), we obtain,

$$H_{mn}\phi_n = -\epsilon_{mij}C_{ijkl}\frac{\partial u_l}{\partial x_k}, \ H_{mn} = H_{nm} = I\omega^2\delta_{mn} - \epsilon_{mij}C_{ijkl}\epsilon_{nkl}. \tag{12}$$

We have $\det(\mathbf{H}) = 0$ for some frequencies, ω_r, which correspond to the cut-off frequencies of optical modes of the micropolar material. For frequencies other than the cut-off frequency $\omega \neq \omega_r$, the micro-rotation can be solved from Eq. (12). Substituting the solved micro-rotation into Eq. (10) yields

$$-\omega^2\rho u_i = \frac{\partial \sigma_{ji}}{\partial x_j}, \ \sigma_{ij} = C^{\text{eff}}_{ijkl}\frac{\partial u_l}{\partial x_k}, \ C^{\text{eff}}_{ijkl} = C_{ijkl} + H^{-1}_{nm}C_{ijrs}\epsilon_{rsn}\epsilon_{mpq}C_{pqkl}. \tag{13}$$

One can see that the micropolar Eq. (13) exactly matches the equation of the asymmetric elasticity Eq. (2). Additionally, the effective tensor C^{eff}_{ijkl} shares the same major symmetry as the target tensor $C^{'}_{ijkl}$ defined in Eq. (2). As a result, one can effectively realize the required asymmetric elastic tensor, $C^{\text{eff}}_{ijkl} = C^{'}_{ijkl}$, by properly selecting the tensor C_{ijkl}. The effective asymmetric elasticity tensor C^{eff}_{ijkl} is frequency dependent or dispersive. We remark that Eq. (13) for balance of linear momentum is only one part of the complete dynamics equation for the micropolar material. It is this part that shares the same form with Eq. (2) for asymmetric transformation elasticity. A complete description of the dynamics of the micropolar material must be supplemented by the balance law for angular momentum Eq. (12). Otherwise, we will face the same issue as the asymmetric elasticity theory, i.e., the unbalanced

angular momentum caused by asymmetric stresses.

By comparing the effective elastic parameters, C^{eff}_{ijkl}, with asymmetric elastic parameters C'_{ijkl} given in Eq. (5), we obtain the following micropolar parameters that can mimic the asymmetric elastic parameters

$$\begin{cases} \rho = \dfrac{\rho_0}{F_{11}F_{22}}, \quad I > 0, \quad A_{ijkl} = 0, \quad D_{ijkl} = 0, \\ C_{11} = \eta(\lambda_0 + 2\mu_0), \quad C_{22} = \dfrac{(\lambda_0 + 2\mu_0)}{\eta}, \quad C_{12} = \lambda_0, \\ C_{66} = \eta\mu, \quad C_{99} = \dfrac{\mu}{\eta}, \quad C_{69} = \mu, \quad \mu = \dfrac{\mu_0 I\omega^2\eta}{\mu_0(\eta-1)^2 + I\omega^2\eta}. \end{cases} \tag{14}$$

The micro-rotation inertia parameter $I > 0$ can be chosen arbitrarily. The required micropolar material has an soft mode resulting from $C_{66}C_{99} - C_{69}^2 = 0$. Mathematically, one can characterize the soft mode as $(0 \quad 0 \quad 1 \quad -\eta)^{\mathrm{T}}$, which stands for a linear combination of pure shear and rotation. A metamaterial example with such soft mode is presented in next section (see Figs. 2 and 3). It is noted that the three shear parameters, C_{66}, C_{99}, andC_{69}, depend on the desired working frequency. When the micro-rotation inertia I becomes very large, the effective parameters tend to become approximately frequency independent. In such a case, a designed micropolar material can approximate an asymmetric elastic material over a broad frequency range. Furthermore, if an external torque is applied to constrain the micro-rotation to zero, the micropolar material can be regarded as a nondispersive asymmetric elastic material. This is equivalent to a previous 2D broadband elastic cloak, in which the rotation of the inner block in each unit cell was externally constrained to zero [25]. For realizing 3D asymmetric transformation, the required micropolar parameters are given in **Appendix A**. In the following, we demonstrate how to achieve such extremal micropolar material.

3. Design of the extremal micropolar material

While the micropolar parameters required for asymmetric transformation elasticity have been theoretically determined, the key challenge lies in constructing an extremal micropolar material that realizes these parameters. In this section, we begin by analyzing the deformation modes of a 2D reduced Cosserat medium. The strain energy of the required micropolar medium is expressed as a quadratic form of these modes, thereby identifying the physical meaning of the third soft mode in addition to curvatures. Based on this understanding, we design a discrete lattice metamaterial whose deformation mechanisms accommodate the required soft modes. By tuning the geometric and material properties of the unit cell, the desired effective micropolar parameters can be achieved. To validate the wave manipulation capability of the proposed metamaterial, we compare its band structure with that of the target micropolar medium, and perform full-wave simulations to confirm its ability to match elastic waves in a background Cauchy medium.

3.1. Deformation modes of extremal micropolar materials

In this section, we discuss soft modes of the above extremal micropolar media. The discussion can provide a guideline for designing soft modes. The required 2D extremal micropolar material for cloaking exhibit two types of soft modes. The first type is related to the vanishing higher-order elasticity tensor $A_{ijkl} = 0$. From the constitutive law, $A_{ijkl} = 0$ means that the gradient of micro-rotation should not induce couple stress. In other words, a nonzero micro-rotation of a material particle should not induce micro-rotation of its neighboring particles. For a metamaterial model based on mass blocks and linear Hooke's springs, as shown in next subsection, it is required that all springs must be coupled to geometry centers of those mass blocks.

As we have noted above, the second type of soft modes is represented by micropolar strain, resulting from $C_{66}C_{99} - C_{69}^2 = 0$ in Eq. (14). Before

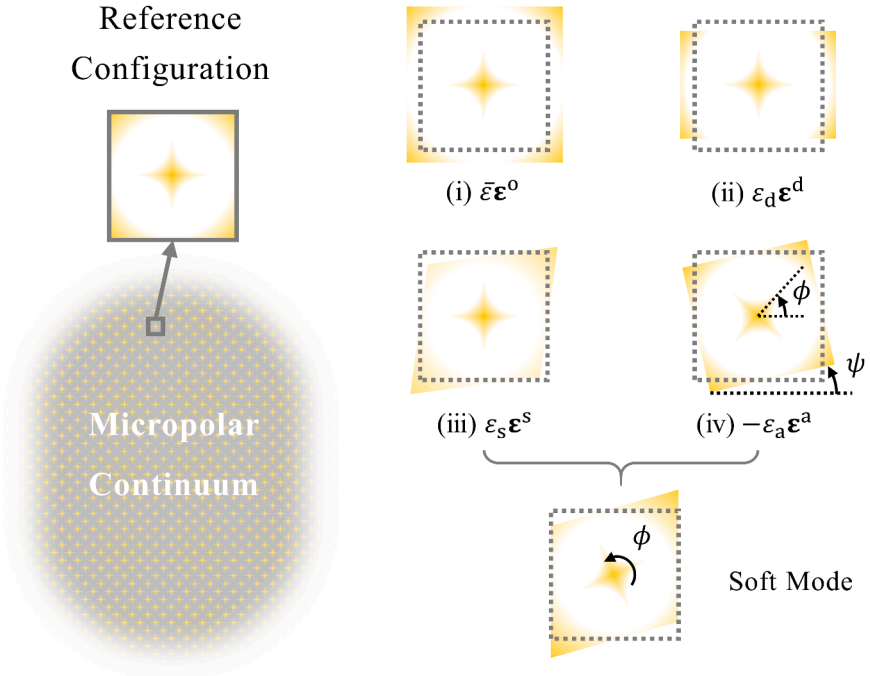

Fig. 2. Four basic deformation modes represented by the micropolar strain tensor, $\boldsymbol{\varepsilon}$. A Cartesian coordinate with two orthonormal bases, $\mathbf{e}_1$ and $\mathbf{e}_2$, is defined. A general micropolar strain $\boldsymbol{\varepsilon}$ can be decomposed into four basic deformation modes: (i) the hydrostatic deformation $\bar{\varepsilon}\boldsymbol{\varepsilon}^{\mathrm{o}} = (u_{1,1} + u_{2,2})(\mathbf{e}_1 \otimes \mathbf{e}_1 + \mathbf{e}_2 \otimes \mathbf{e}_2)/2$, (ii) the first pure shear mode $\varepsilon_{\mathrm{d}}\boldsymbol{\varepsilon}^{\mathrm{d}} = (u_{1,1} - u_{2,2})(\mathbf{e}_1 \otimes \mathbf{e}_1 - \mathbf{e}_2 \otimes \mathbf{e}_2)/2$, (iii) the second pure shear mode $\varepsilon_s\boldsymbol{\varepsilon}^{\mathrm{s}} = (u_{1,2} + u_{2,1})(\mathbf{e}_1 \otimes \mathbf{e}_2 + \mathbf{e}_2 \otimes \mathbf{e}_1)/2$, and (iv) the pure rotation mode $-\varepsilon_{\mathrm{a}}\boldsymbol{\varepsilon}^{\mathrm{a}} = (\phi - \psi)(\mathbf{e}_1 \otimes \mathbf{e}_2 - \mathbf{e}_2 \otimes \mathbf{e}_1)$, with $\psi = (u_{2,1} - u_{1,2})/2$ being the displacement-induced macro-rotation. For the extremal micropolar material in Eq. (14), the soft mode is a combination of a shear and the pure rotation, as shown here.

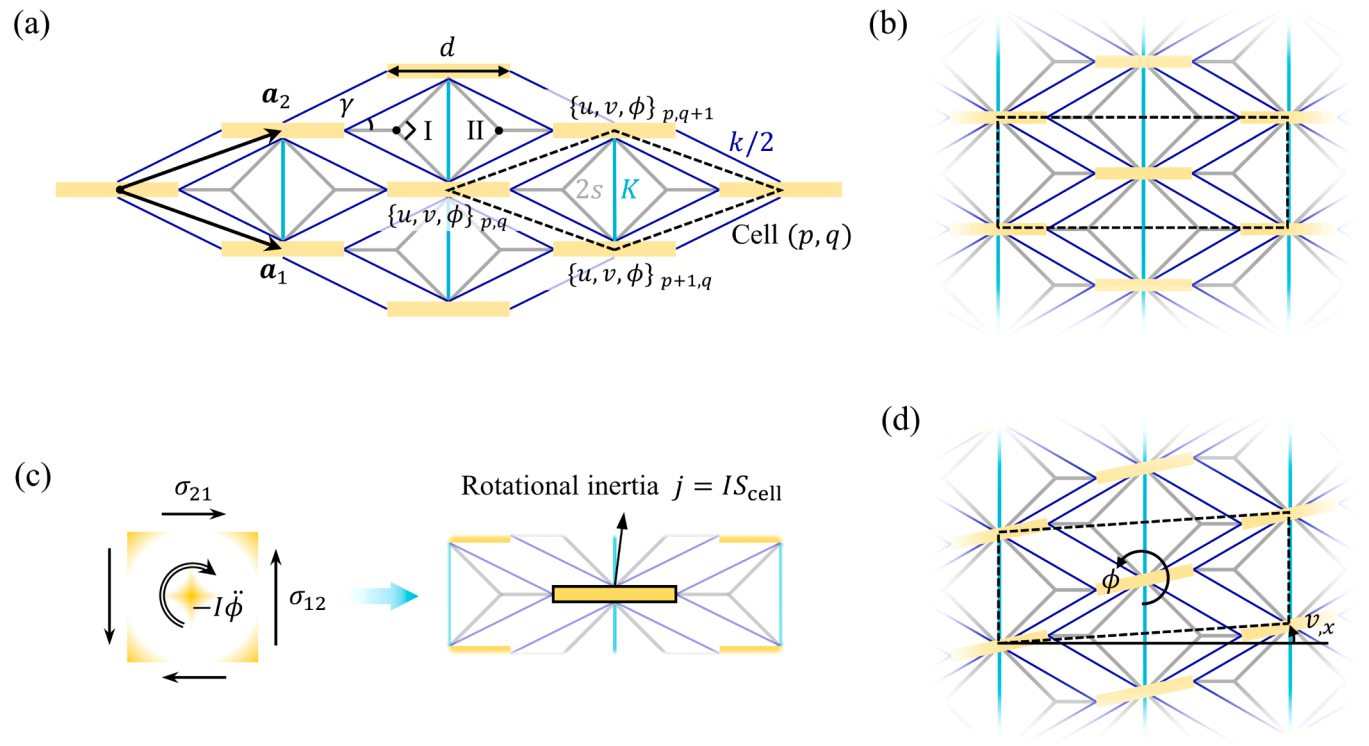

Fig. 3. A metamaterial model for realizing extremal micropolar materials. (a) The metamaterial is consisted of rigid mass blocks (yellow rectangles) and massless springs (blue, gray and cyan lines). In physical realizations, such spring-like elements can be approximated by thin beam structures. Geometry parameters and spring constants are indicated. The gray springs have two massless common nodes, I and II. (b) A rectangular unit cell (highlighted by the dashed box) of the metamaterial in (a). (c) The equivalence between the micropolar medium unit cell and the metamaterial unit cell, where $\phi_{p,q} = \phi$ and $j = IS_{\text{cell}}$. (d) Illustration of a soft mode of the metamaterial within the linear approximation. The mode is composed of shear and pure rotation.

getting into the detail, we first provide a schematic of all possible deformation modes (not necessary be soft modes) related to the strain tensor. In general, we can decompose a micropolar strain tensor (2D case) into the following four parts, corresponding to four basic deformation modes

$$\boldsymbol{\varepsilon} = \nabla\mathbf{u} - \phi\boldsymbol{\varepsilon}^{\mathrm{a}} = \bar{\varepsilon}\boldsymbol{\varepsilon}^{\mathrm{o}} + \varepsilon_{\mathrm{d}}\boldsymbol{\varepsilon}^{\mathrm{d}} + \varepsilon_{\mathrm{s}}\boldsymbol{\varepsilon}^{\mathrm{s}} + \varepsilon_{\mathrm{a}}\boldsymbol{\varepsilon}^{\mathrm{a}} \tag{15}$$

in which,

$$\begin{cases} \boldsymbol{\varepsilon}^{\mathrm{o}} = \mathbf{e}_1 \otimes \mathbf{e}_1 + \mathbf{e}_2 \otimes \mathbf{e}_2, & \bar{\varepsilon} = \dfrac{u_{1,1} + u_{2,2}}{2}, \\ \boldsymbol{\varepsilon}^{\mathrm{d}} = \mathbf{e}_1 \otimes \mathbf{e}_1 - \mathbf{e}_2 \otimes \mathbf{e}_2, & \varepsilon_{\mathrm{d}} = \dfrac{u_{1,1} - u_{2,2}}{2}, \\ \boldsymbol{\varepsilon}^{\mathrm{s}} = \mathbf{e}_1 \otimes \mathbf{e}_2 + \mathbf{e}_2 \otimes \mathbf{e}_1, & \varepsilon_{\mathrm{s}} = \dfrac{u_{1,2} + u_{2,1}}{2}, \\ \boldsymbol{\varepsilon}^{\mathrm{a}} = \mathbf{e}_1 \otimes \mathbf{e}_2 - \mathbf{e}_2 \otimes \mathbf{e}_1, & \varepsilon_{\mathrm{a}} = \dfrac{u_{2,1} - u_{1,2}}{2} - \phi, \end{cases} \tag{16}$$

with $\mathbf{e}_1$ and $\mathbf{e}_2$ representing two orthogonal bases of the coordinate system. One can verify that the four tensors,$\boldsymbol{\varepsilon}^{\mathrm{o}}$, $\boldsymbol{\varepsilon}^{\mathrm{d}}$,$\boldsymbol{\varepsilon}^{\mathrm{s}}$, and $\boldsymbol{\varepsilon}^{\mathrm{a}}$ are orthogonal to each other. $\bar{\varepsilon}\boldsymbol{\varepsilon}^{\mathrm{o}}$, $\varepsilon_{\mathrm{d}}\boldsymbol{\varepsilon}^{\mathrm{d}}$, and $\varepsilon_{\mathrm{s}}\boldsymbol{\varepsilon}^{\mathrm{s}}$ in together represents the symmetric part of the micropolar strain tensor, i.e., $\bar{\varepsilon}\boldsymbol{\varepsilon}^{\mathrm{o}} + \varepsilon_{\mathrm{d}}\boldsymbol{\varepsilon}^{\mathrm{d}} + \varepsilon_{\mathrm{s}}\boldsymbol{\varepsilon}^{\mathrm{s}} = (\nabla\mathbf{u} + \mathbf{u}\nabla)/2$. The asymmetric part of the strain tensor is exclusively represented by $\varepsilon_{\mathrm{a}}\boldsymbol{\varepsilon}^{\mathrm{a}}$. We refer $-\varepsilon_{\mathrm{a}}$ as the pure rotation [75] because it represents the difference between the micro-rotation, ϕ, and the displacement-related macro-rotation $(\nabla\mathbf{u}{:}\boldsymbol{\varepsilon}^{\mathrm{a}})/2$. We schematically represent in Fig. 2 the four deformation modes based on an infinitesimal square element. As expected, $\bar{\varepsilon}$ corresponds to a hydrostatic deformation, omnidirectional expansion or omnidirectional compression. Both ε_{d} and ε_{s} represent a pure shear mode though the deformation for ε_{d} is quite different from that of ε_{s} at first sight (compare (ii) and (iii) in Fig. 2). The mode for ε_{d} becomes the same as ε_{s} if one represent ε_{d} in a coordinate that is rotated by 45°. The pure rotation mode, $-\varepsilon_{\mathrm{a}}$, is also schematically represented.

The above four modes themselves can be soft modes or their combinations can be soft modes. The soft mode of the extremal micropolar material with the parameters in Eq. (14) belongs to the latter case. The soft mode can be identified by analyzing the strain energy density

$$w = \frac{1}{2}\boldsymbol{\varepsilon} : \mathbf{C} : \boldsymbol{\varepsilon} = P\bar{\varepsilon}^2 + Q\varepsilon_{\mathrm{d}}^2 + R\bar{\varepsilon}\varepsilon_{\mathrm{d}} + \frac{\mu}{2\eta}[(1+\eta)\varepsilon_{\mathrm{s}} - (1-\eta)\varepsilon_{\mathrm{a}}]^2,$$
$$P = \frac{(1+\eta)^2\lambda_0 + 2(1+\eta^2)\mu_0}{2\eta}, \quad Q = \frac{(1-\eta)^2\lambda_0 + 2(1+\eta^2)\mu_0}{2\eta}, \quad R = \frac{(\eta^2-1)(\lambda_0 + 2\mu_0)}{2\eta}. \tag{17}$$

From the last term, we identify a soft mode that is a linear combination of shear and pure rotation, characterized by $\bar{\varepsilon} = \varepsilon_{\mathrm{d}} = 0$ and $\varepsilon_{\mathrm{s}}/\varepsilon_{\mathrm{a}} = (1-\eta)/(1+\eta)$. This soft mode is a direct consequence of the rank-

deficiency of the elasticity tensor C_{ijkl} discussed earlier, i.e., $C_{66}C_{99} - C_{69}^2 = 0$. Therefore, the following proposed metamaterial must allow this soft mode.

3.2. An extremal micropolar metamaterial model

Here, we propose a discrete metamaterial model (Fig. 3(a)) to realize the above extremal micropolar material. Two lattice vectors of the metamaterial are defined as $\mathbf{a}_1 = \{l, -h\}^{\mathrm{T}}$ and $\mathbf{a}_2 = \{l, +h\}^{\mathrm{T}}$, respectively. Each unit cell contains a mass block (yellow rectangle) with mass M and length d. The width of the mass block is assumed to be negligible. These mass blocks are coupled to their neighbors by linear Hooke's springs. A zoom-in view of a single unit cell is shown in Fig. 3(c), where the central yellow rectangular block has one rotational and two translational DOFs. The micro-rotation inertia originates from this rotational DOF and is important for balancing the asymmetric shear stress. In later derivation, the volume average of the rotational inertia j of the yellow block serves as the effective micro-rotation inertia. As the width of the mass blocks is negligible, one can image that the rotation of any mass block doesn't cause rotation of its neighbors. This is consistent with the requirement by a vanishing higher-order elasticity tensor. The specific angle γ, the blue springs with spring constant $k/2$, and the vertical cyan springs with spring constant K enable us to adjust the anisotropy of the effective elasticity tensor. Furthermore, the gray springs with spring constant $2s$ serve to tune C_{12} independently.

We consider a rectangular unit cell (Fig. 3(b)) to illustrate the soft mode of the metamaterial more intuitively. First, an affine displacement represented by $u_{,x} = u_{,y} = v_{,y} = 0$, $v_{,x} > 0$ is assumed for all mass blocks. Then, all mass blocks are rotated by the same angle ϕ. The total deformation is indicated in Fig. 3(d). It can be checked that all springs exhibit zero stretching if $\phi d/2 = l v_{,x}$ and we thus obtain an soft mode of the metamaterial. According to Eq. (16), the soft mode is represented by $\bar{\varepsilon} = \varepsilon_{\mathrm{d}} = 0, \varepsilon_{\mathrm{s}} = v_{,x}/2$, and $\varepsilon_{\mathrm{a}} = v_{,x}/2 - \phi = (1 - 4l/d)\varepsilon_{\mathrm{s}}$, which is exactly a combination of shear and pure rotation, as indicated by Eq. (17). It should be noted that the metamaterial has a stretching ratio $\eta = 2l/(2l - d) > 1$. One can simply rotate the metamaterial by 90° if an asymmetric elastic material with $\eta < 1$ is needed. In the above discussion, we use ϕ to denote the rotation of the mass block, implying that the rotation of the mass block corresponds to the micro-rotation ϕ of its equivalent micropolar medium. In Fig. 3(c), we illustrate the equivalence between the micropolar continuum unit cell and the metamaterial unit cell. The volume average of the rotational inertia j of the mass block serves as the effective micro-rotation inertia, and the resulting inertial torque is used to balance the asymmetric stresses.

In the following, we derive effective micropolar continuum parameters of the proposed metamaterial following a previous procedure [75]. We denote the displacement and rotation of each mass block as $\mathbf{u}_{p,q} = \{u_{p,q}, v_{p,q}\}^{\mathrm{T}}$ and $\phi_{p,q}$, respectively. We assume all displacements and rotations to be infinitesimal, i.e., in a linear elastic range. The kinetic energy of the unit cell (p, q) can be expressed as

$$K_{p,q} = \frac{1}{2}M\left|\dot{\mathbf{u}}_{p,q}\right|^2 + \frac{1}{2}j\dot{\phi}_{p,q}^2. \tag{18}$$

The moment of inertia of the mass block with negligible thickness is $j = Md^2/12$. The displacements of the left and right end-points of the mass block in the unit cell (p, q) are expressed as

$$u_{p,q}^{\mathrm{L}} = \left\{u_{p,q}, v_{p,q} - \frac{\phi_{p,q}d}{2}\right\}^{\mathrm{T}},\ u_{p,q}^{\mathrm{R}} = \left\{u_{p,q}, v_{p,q} + \frac{\phi_{p,q}d}{2}\right\}. \tag{19}$$

The displacements of the hidden massless nodes I and II (see Fig. 3(a)) are assumed to be $\mathbf{u}_{p,q}^{\mathrm{I}}$ and $\mathbf{u}_{p,q}^{\mathrm{II}}$ respectively. We obtain the potential energy, $U_{p,q}$, for the unit cell (p, q) by summing up the elastic energies of the 11 springs inside the unit cell. The expression is neglected here due to lengthy expression.

Then, we derive the Lagrangian of the system

$$L = \sum_{p,q}\left(K_{p,q} - U_{p,q}\right). \tag{20}$$

The governing equations of the system are obtained as

$$\frac{\partial}{\partial t}\left(M\dot{u}_{p,q}\right) = \frac{\partial L}{\partial u_{p,q}}, \frac{\partial}{\partial t}\left(M\dot{v}_{p,q}\right) = \frac{\partial L}{\partial v_{p,q}}, \frac{\partial}{\partial t}\left(j\dot{\phi}_{p,q}\right) = \frac{\partial L}{\partial \phi_{p,q}}. \tag{21}$$

For the hidden DOFs $\mathbf{u}_{p,q}^{\mathrm{I}}$ and $\mathbf{u}_{p,q}^{\mathrm{II}}$, we have

$$\frac{\partial L}{\partial u_{p,q}^{\mathrm{I}}} = 0, \quad \frac{\partial L}{\partial v_{p,q}^{\mathrm{I}}} = 0, \quad \frac{\partial L}{\partial u_{p,q}^{\mathrm{II}}} = 0, \quad \frac{\partial L}{\partial v_{p,q}^{\mathrm{II}}} = 0, \tag{22}$$

Substituting the displacements of the hidden nodes solved from Eq. (22) into Eq. (21) yields the final governing equations in terms of the DOFs of the mass blocks.

The above derived governing equation is a discrete version. We consider the following Taylor series in order to obtain a continuum micropolar model. Since each mass block is only coupled to its nearest neighbors (see Fig. 3(a)), we expand $u_{p+m,q+n}$ with $m, n = -1, 0, +1$ to a second order

$$u_{p+m,q+n} = u_{p,q} + \left(\frac{\partial u}{\partial \mathbf{x}}\right)^{\mathrm{T}} \mathrm{d}\mathbf{x}_{m,n} + \frac{1}{2}\mathrm{d}\mathbf{x}_{m,n}^{\mathrm{T}}\frac{\partial^2 u}{\partial \mathbf{x}^2}\mathrm{d}\mathbf{x}_{m,n} + O\left(\left|\mathrm{d}\mathbf{x}_{m,n}\right|^3\right), \tag{23}$$

where $\mathrm{d}\mathbf{x}_{m,n} = m\mathbf{a}_1 + n\mathbf{a}_2$. $v_{p+m,q+n}$ and $\phi_{p+m,q+n}$ can be expanded similarly. Substitution of the expansion into Eq. (21) yields in the following micropolar elasticity equations

where the parameters are,

$$\begin{cases} \rho\ddot{u} = C_{11}u_{,xx} + C_{99}u_{,yy} + (C_{12} + C_{69})v_{,xy} + (C_{99} - C_{69})\phi_{,y}, \\ \rho\ddot{v} = C_{66}v_{,xx} + C_{22}v_{,yy} + (C_{12} + C_{69})u_{,xy} + (C_{69} - C_{66})\phi_{,x}, \\ I\ddot{\phi} = A_{11}\phi_{,xx} + A_{22}\phi_{,yy} + 2A_{12}\phi_{,xy} + (C_{66} - C_{69})v_{,x} + (C_{69} - C_{99})u_{,y} + (2C_{69} - C_{66} - C_{99})\phi, \end{cases} \tag{24}$$

$$\begin{cases} \rho = \dfrac{M}{S_{\mathrm{cell}}}, \quad I = \dfrac{j}{S_{\mathrm{cell}}}, \quad S_{\mathrm{cell}} = 2lh, \quad A_{11} = A_{12} = A_{21} = A_{22} = 0, \\ C_{11} = \dfrac{l}{h}\left(s + k\cos^2\gamma\right), \quad C_{22} = \dfrac{h}{l}\left(s + k\sin^2\gamma + 2K\right), \\ C_{66} = \dfrac{l}{h}k\sin^2\gamma, \quad C_{99} = \dfrac{h}{l}k\cos^2\gamma, \\ C_{12} = s + k\sin\gamma\cos\gamma, \quad C_{69} = k\sin\gamma\cos\gamma. \end{cases} \tag{25}$$

As anticipated, the effective micropolar medium indeed has a zero higher-order elasticity tensor $\mathbf{A} = \mathbf{0}$ and the condition $C_{66}C_{99} - C_{69}^2 = 0$ is also satisfied. In order to obtain the desired extremal micropolar parameters in Eq. (14), we derive the following model parameters

$$\begin{cases} M=\dfrac{\rho_0 S_{\text{cell}}}{F_{11}F_{22}}, \quad s=\lambda_0-\mu, \quad k=\dfrac{\mu}{\sin\gamma\cos\gamma}, \\ K=\dfrac{(\lambda_0+2\mu_0)\cot\gamma-k\sin^2\gamma-(\lambda_0-\mu)}{2}, \\ \gamma=\operatorname{arccot}\left(\dfrac{\sqrt{(\lambda_0-\mu)^2+4\mu(\lambda_0+2\mu_0)}-(\lambda_0-\mu)}{2\mu}\right). \end{cases} \tag{26}$$

It should be mentioned that the geometry requirement of $\arctan(h/l)<\gamma<\pi/4$ (see Fig. 3(a)) imposes limitation to the available extremal micropolar parameters. Specifically, the Poisson's ratio of the background material must be positive $\nu>0$, otherwise, the required micropolar parameters in Eq. (14) cannot be achieved with the proposed metamaterial.

3.3. Verification of the extremal micropolar metamaterial

Next, we demonstrate that the proposed micropolar metamaterial can be used for controlling elastic waves based on asymmetry transformation elasticity. For simplicity, we consider a compression mapping denoted by $F_{11}=2/3$ and $F_{22}=1$. Elastic parameters of the background Cauchy material are taken as $\lambda_0=2\mu_0=110\text{GPa}$ and $\rho_0=2.4\times10^3\text{kg/m}^3$, arbitrarily. We consider an operating frequency $f_{\text{ext}}=\omega_{\text{ext}}/(2\pi)=6300\text{Hz}$. The metamaterial cell should be sufficiently small compared to the shear wavelength in the background material, i.e., $2l\ll c_{\text{T}}/f_{\text{ext}}$, where $c_{\text{T}}=\sqrt{\mu_0/\rho_0}$. Here, we choose the unit cell size $l=(c_{\text{T}}/f_{\text{ext}})/2N$ with $N=10$. The geometry and material parameters for the metamaterial model follows Eq. (26),

$$\begin{cases} M=3.52\text{ kg}, \quad s=1.08\times10^{11}\text{ N/m}, \quad k=4.34\times10^{9}\text{ N/m}, \\ K=1.62\times10^{11}\text{ N/m}, \\ l=3.80\text{ cm}, \quad h=1.29\text{ cm}, \quad d=2.53\text{ cm}. \end{cases} \tag{27}$$

To illustrate the wave characteristics of this metamaterial and its corresponding micropolar continuum, we derive their dispersion relations by applying the Bloch-Floquet ansatz $\mathbf{u}_{p+m,q+n}=\mathbf{u}_{p,q}\exp(\mathrm{i}\mathbf{k}\cdot(m\mathbf{a}_1+n\mathbf{a}_2))$, with $\mathbf{u}_{p,q}=\widehat{\mathbf{u}}_{p,q}\exp(-\mathrm{i}\omega t)$, and the harmonic wave assumption $\mathbf{u}=\widehat{\mathbf{u}}\exp(\mathrm{i}(\mathbf{k}\cdot\mathbf{x}-\omega t))$ into Eq. (21) and Eq. (24), respectively [75]. There are two acoustic bands related to the two displacement DOFs. In addition, we obtain a micro-rotation dominated optical branch, with a cut-off frequency, $\omega_{\text{r}}=3.89\times10^4\text{rad/s}$. The three bands obtained from the continuum model (red lines in Fig. 4(a)) and those from the microstructure lattice (chain lines in Fig. 4(a)) show good agreement in the long-wavelength limit, i.e., around the Γ point. Since the Taylor expansion Eq. (23) is more accurate for small wave numbers, we observe a larger discrepancy between the two results for larger wavenumbers, especially along two principal directions of the micropolar material, i.e., the ΓX direction and ΓY direction. Along the two principal directions, the shear branch for the continuum model exhibits zero frequency due to the above explained soft mode of the metamaterial. Therefore, at low frequency range, only one bulk longitudinal mode can propagate along these two directions. The transverse and optical modes are coupled, while the longitudinal mode and the optical mode are decoupled (see Fig. 4(b)). At a certain wavenumber along both

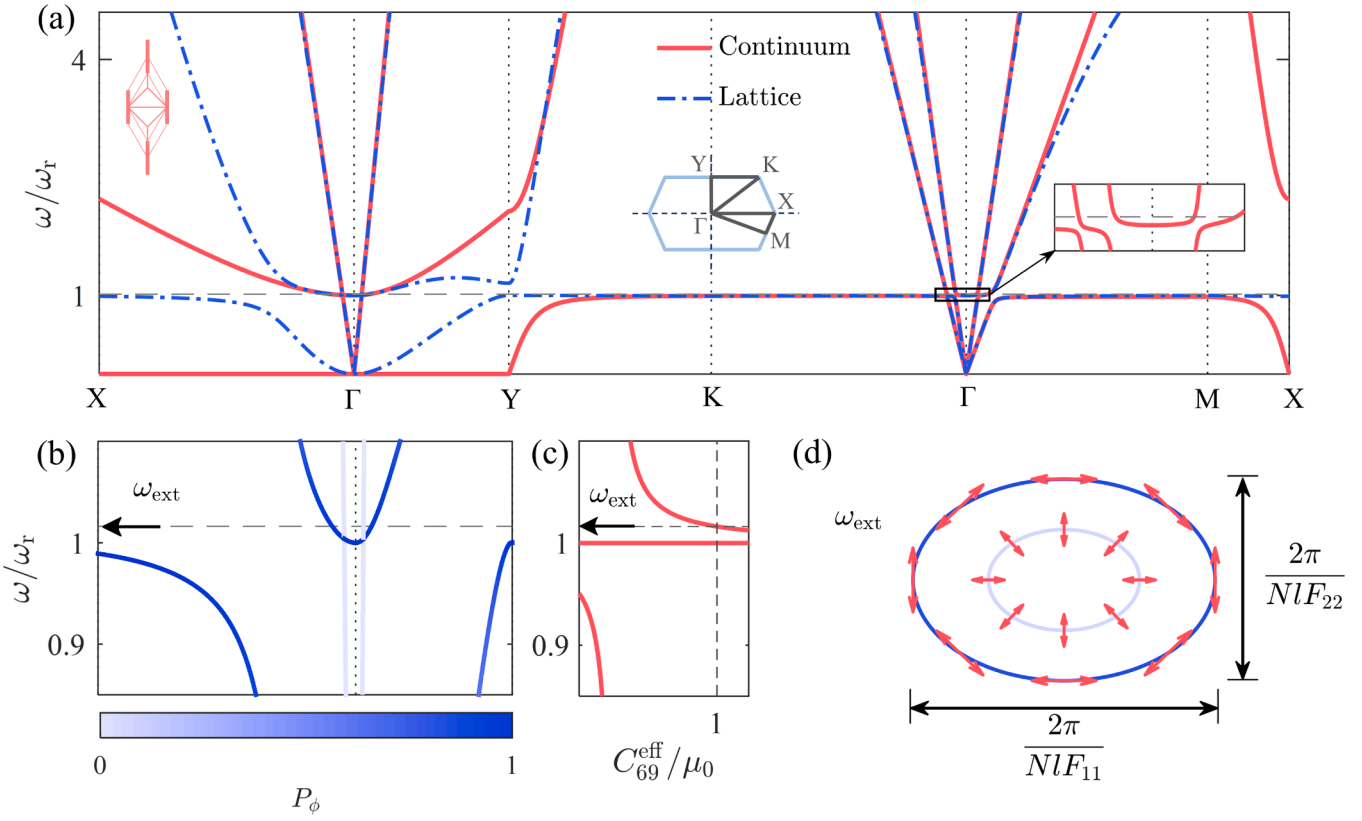

Fig. 4. (a) Dispersion bands calculated from the micropolar continuum model (red solid line) and the proposed microstructure lattice (blue chain line). The insets show a unit cell of the metamaterial (top-left), the first Brillouin zone (center) and an enlarged view of the lifted degeneracy (right). (b) Zoomed-in view of the band structure of the lattice near the operating frequency ω_{ext} along the path X – Γ – Y. The contribution of micro-rotation to each mode, characterized by $P_\phi=j\widehat{\phi}^2/(M\widehat{u}^2+M\widehat{v}^2+j\widehat{\phi}^2)$, are encoded by color. Dark blue indicates strong participation of micro-rotation while light blue means micro-rotation is negligible in the mode. (c) Effective relative shear modulus C_{69}^{eff}. (d) Iso-frequency contour of the metamaterial at the operating frequency ω_{ext}. Displacement polarization of the modes are represented by red double arrows.

directions, the longitudinal and optical branches become degenerate, exhibiting identical frequencies. However, for wave propagating along directions other than the two principal directions, such as the ΓK direction and ΓM direction, the transverse mode, longitudinal mode and optical mode all couple together, leading to a non-zero-frequency transverse branch and a lifted degeneracy (or the degeneracy is broken) between the longitudinal branch and the optical branch. As result, the degeneracy along the two principal directions forms a Dirac cone [93], i.e., two frequency surfaces touch at a point, in similar to two cones contacting at their cone-tips. It is interesting that the micropolar continuum calculation perfectly reproduce the Dirac cone of the metamaterial. The micropolar elasticity can potentially provide an continuum route to investigate Dirac physics [94].

The dashed gray line in Fig. 4(b) indicates the operating frequency ω_{ext} of the designed metamaterial. Here, the metamaterial supports two propagating modes, which are necessary to match the longitudinal and transverse modes of the background material. The effective shear modulus C_{69}^{eff} at the operating frequency ω_{ext} matches the shear modulus of the background material (see Fig. 4(c)). At the operating frequency, ω_{ext}, the iso-frequency contour of the metamaterial are two ellipses with the same aspect ratio as the stretching ratio $\eta = 2/3$. This is necessary for perfectly matching the wave property of the background material, as demonstrated in a previous asymmetric elastic metamaterial [29]. A notable difference between our current metamaterial and the previous one [29] is that we here exploit an acoustical mode and an optical mode, while the previous design relies on two optical modes.

Next, we verify in COMSOL Multiphysics that the wave property of the above extremal micropolar metamaterial. Specifically, we consider a metamaterial slab consisting of 24 layers, with a total thickness of $48h$, sandwiched in the background Cauchy medium (Fig. 5(a)). The background Cauchy medium is modeled by using the Solid Mechanics module. The mass blocks and the springs in the metamaterial are modeled by using the Beam module in COMSOL Multiphysics, respectively. We couple the background Cauchy continuum and the metamaterial slab at their interface by imposing pointwise displacement continuity to corresponding nodes of the two regions. The simulation frequency is set to be the operating frequency $f_{\text{ext}} = 6300\text{Hz}$. We show in Fig. 5(a) the simulated displacement fields for a Gaussian beam incident onto the micropolar matching layer at an angle of 45°. The incident wave is perfectly transmitted through the matching layer, with negligible wave scattering or reflection. The wave fields inside the matching layer are compressed by a factor of $F_{11} = 2/3$. The energy flow direction and the wavevector inside the matching layer are in agreement with the iso-frequency curve analysis (see Fig. 5(b) and (c)). Furthermore, the matching layer should be valid for arbitrary incidence angles. This can be verified by simulating an incident cylindrical wave, which consists of plane waves along all propagation directions in 2D space. Nearly perfect transmission for the incident cylindrical wave is observed, either for the transverse case (Fig. 5(d)) or the longitudinal case (Fig. 5(f)).

We also simulate the micropolar matching layer by using the derived effective micropolar continuum parameters in Eq. (25). The micropolar elasticity equation is implemented in weak form in COMSOL Multiphysics [84]. In the simulation, we assume that both the surface traction and the surface couple stress is continuous at the interface separating the background Cauchy medium and the micropolar continuum. The continuity equations can be derived by analyzing the balance of linear momentum and angular momentum for an infinitely thin strip containing the interface. The displacement is also supposed to be continuous at the interface, resulting from a perfect bonding between the two media, while the micro-rotation of the micropolar medium at the interface is not constrained. The micropolar continuum calculations (Fig. 5(e) and (g)) show a perfect transmission of the incident wave. The

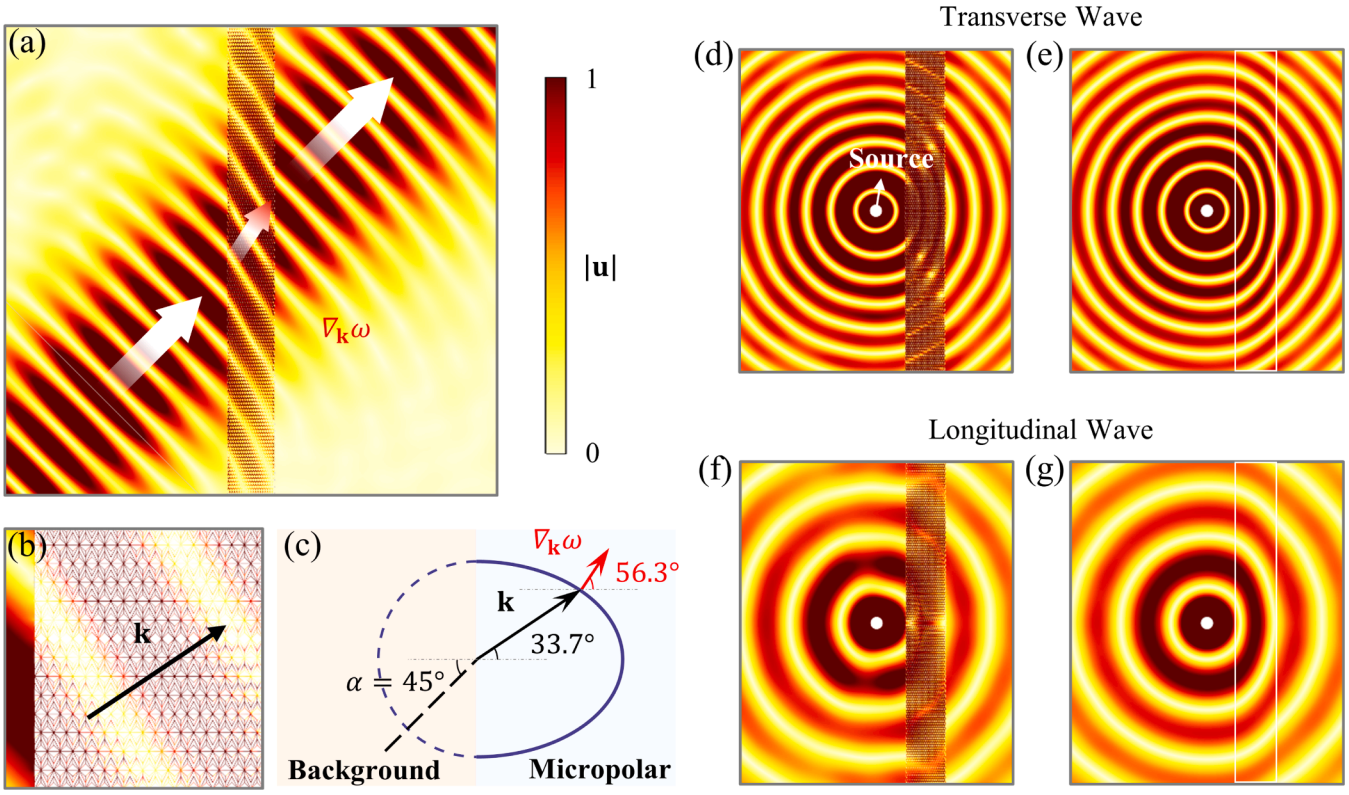

Fig. 5. Simulation of a micropolar matching layer with different incident waves. (a) Displacement fields for a transverse polarized Gaussian beam obliquely incident onto the micropolar matching layer. Colors stand for the displacement magnitude $|\mathbf{u}|$. Arrows are for energy flow directions. (b) Zoomed-in view and the wave vector. (c) Iso-frequency contour of the background Cauchy material and the micropolar metamaterial at the operating frequency, ω_{ext}. (d), (e) Results for the metamaterial and an effective micropolar continuum with an incident transverse cylindrical wave. The region enclosed by the white rectangle box represents the micropolar continuum medium. (f) (g) Same as (d), (e) but for an incident longitudinal cylindrical wave.

above simulations intuitively demonstrate that the proposed extremal micropolar metamaterial behaves as its effective micropolar continuum, matching the surrounding Cauchy medium and achieving compression of elastic wave fields.

It is important to note that the adopted homogenization method for the micropolar metamaterial is valid in the long-wavelength limit. Therefore, the metamaterial unit cell should be sufficiently small, or alternatively each shear wavelength should contain $N \geq 10$ metamaterial unit cells. To reduce the required number of unit cells per wavelength, one may adopt the enhanced homogenization method that remain valid far away from the Γ point [79]. This approach could potentially simplify the design of the microstructure cloak in next section, which currently contains 123 layers along the radial direction.

4. Design and verification of 2D micropolar elasticity cloak

Now, we start the design and verification of an elastic cloak based on the proposed extremal micropolar metamaterial. We choose a linear mapping (see Fig. 1(a)), $g(r) = b(r-a)/(b-a) + \delta(r-b)/(a-b)$ in a polar coordinate for the cloak design. The function maps a circular region with a hole, with radius δ, in the virtual space onto an annular cloak with inner radius a and outer radius b in the physical space. Specifically, a position $\mathbf{X} = R\mathbf{e}_R$ in the virtual space is mapped onto a position $\mathbf{x} = r\mathbf{e}_r$ in the physical space with $R = g(r)$ and $\Theta = \theta$. The mapping gradient can then be derived as $\mathbf{F} = \partial\mathbf{x}/\partial\mathbf{X} = 1/g'(r)\mathbf{e}_r\otimes\mathbf{e}_r + r/g(r)\mathbf{e}_\theta\otimes\mathbf{e}_\theta$, with $\mathbf{e}_r$ and $\mathbf{e}_\theta$ being the unit basis vectors along the r- and θ-direction of the polar coordinate. We choose the same background Cauchy material as before, $\lambda_0 = 2\mu_0 = 110$GPa and $\rho_0 = 2.4\times10^3$kg/m^3. The geometry parameters are chosen as $b = 2a = 1$m and $\delta = a/5$. By substituting $\eta(r) = F_{rr}/F_{\theta\theta} = g(r)/(rg'(r))$ into Eq. (14), the required micropolar parameters, dependent on the radial position, can be obtained. The corresponding microstructure parameters are further derived from Eq. (26).

The resulting cloak is consisted of in total $N_r = 123$microstructures layers along the radial direction and $N_\theta = 84$ sectors along the θ direction. We illustrate in Fig. 6(a) the construction process of the metamaterial cloak. The metamaterial unit cells in the cloak are arranged such that the long axis of the mass blocks is along the θ-direction of the polar coordinate since the required $\eta < 1$. The metamaterial unit cell in the outermost layer (or the first layer) has the largest size. We choose $l_1 = (c_T/f_{ext})/2N$ with $N = 10.16$ for the first layer to ensure the long wavelength condition. For all unit cells in the cloak (see Fig. 6(a)), we have replaced the rectangular mass blocks by polyline-shaped blocks to maintain conformation with the polar coordinate. All springs or beams are coupled to mass blocks at corresponding edges. Geometric parameters of the unit cells at the location, r_n, are as indicated. The linear mapping results in a constant length of the mass block, $d = 2\pi b(a-\delta)/N_\theta(b-\delta)$. We have used two angles, γ_n^o and γ_n^i, (see Fig. 6(a)) for each layer. The outer one is chosen as $\gamma_n^o = \arctan(h_{n-1}/(\eta(r_n)l_n))$, while the inner one γ_n^i is derived from the required micropolar properties at that location. The metamaterial cloak is constructed layer by layer from the first layer with the iteration relation $r_n = r_{n-1} - h_{n-1}$ and $h_n = \eta(r_n)l_n\tan(\gamma_n^i)$.

We show in Fig. 6(b) the distribution of the effective micropolar properties of the designed cloak along the radial direction. Due to a very large number of metamaterial layers along the radial direction, the effective parameters (dots) of the metamaterial cloak approximates the continuous parameters (solid lines) required by transformation theory very well. This leads to a good approximation of the microstructure cloak to the theoretical design, as demonstrated below.

We model the microstructure cloak in COMSOL Multiphysics like the simulations in previous Section 3.3. The background material and the metamaterial are modeled by using the Solid Mechanics Module and the Beam Module, respectively. We apply a traction free boundary condition to the inner surface of the cloak. We verify the cloaking performance of the designed elastic cloak by considering a plane wave incident from the left side. The entire simulation domain is surrounded by the Perfectly Matched Layers in COMSOL Multiphysics to avoid undesired reflections from boundaries. We first show the simulated displacement fields for a transverse plane wave (Fig. 7(a)) and a longitudinal plane wave (Fig. 7(e)) onto a circular void. The void induces rather pronounced scattering to the left side and the right side of the void. In sharp contrast, the incident plane wave smoothly propagates through the cloak to the forward region when the void is covered by the microstructure cloak (Fig. 7(b) and (f)). The cloak demonstrates a very satisfying cloaking performance. The displacement fields for the microstructure cloak exhibit quite good consistency with the simulation based on effective micropolar medium (Fig. 6(c) and (g)). We remark that a small radius $\delta = a/5$ is adopted for the cloak design and weak scattering of the cloak is inevitable. As can be seen, the cloaking performance of the cloak is rather close to the theoretical target of a small hole with radius δ (Fig. 6(d) and (h)).

We calculate the total scattering cross-section (TSCS) for the cloak [9] under incident plane transverse and longitudinal waves. The TSCS is defined as the ratio of the scattered power by an object to the incident power density on the object. The displacement and stress fields are decomposed into the incident and scattered components, $\mathbf{u} = \mathbf{u}^{in} + \mathbf{u}^{sc}$ and $\boldsymbol{\sigma} = \boldsymbol{\sigma}^{in} + \boldsymbol{\sigma}^{sc}$, respectively. In the backward region before the target, the scattered waves are equivalent to reflected waves. In the forward region after the target, the superposition of the incident waves and the scattered waves constitutes the transmitted waves. The incident

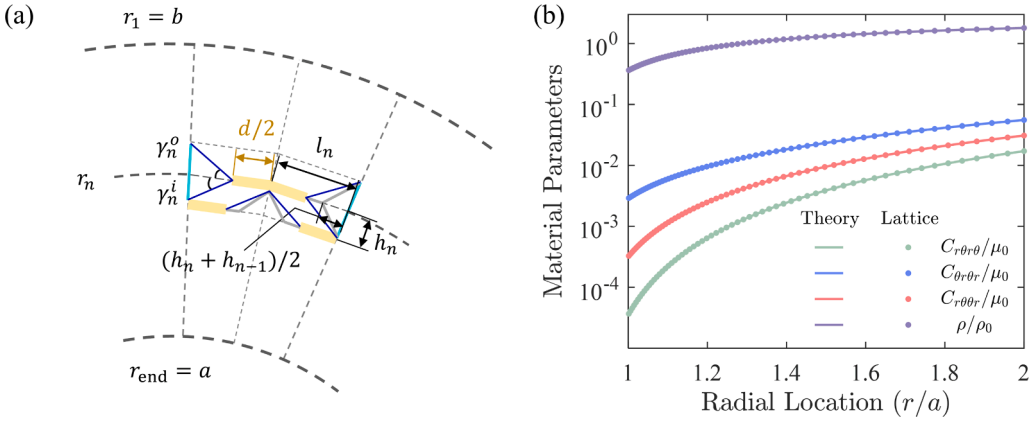

Fig. 6. Microstructure elastic cloak based on extremal micropolar metamaterials. (a) Sketch of the construction process of the microstructure cloak. Geometric parameters of the unit cells in the nth layer are marked. We number the outermost layer as layer 1. (b) Effective micropolar parameters (dots) of each layer along the radial direction for the designed microstructure cloak. We only show the three shear modulus and mass the density for clarity. The designed material properties are in perfect agreement with the micropolar parameters (solid lines) required by cloaking theory.

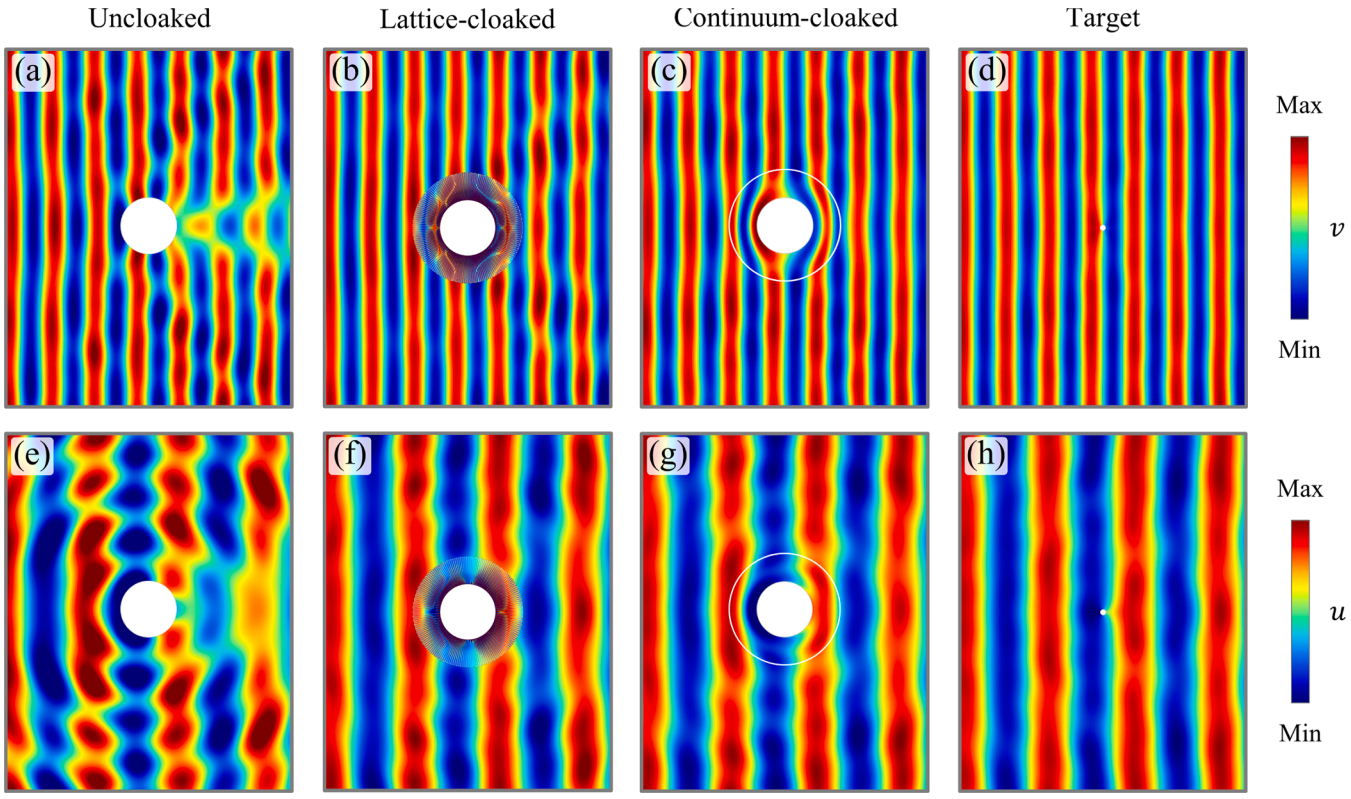

Fig. 7. Verification of the designed cloak based on extremal micropolar metamaterials.(a) Simulated displacement fields, v (vertical component of the displacements), for a transverse plane wave incident from the left side onto a void (inner circular white region) with radius a. (b) Same as (a) but with the void covered by the designed microstructure cloak, with inner radius a and outer radius $b = 2a$. (c) Same as (b) but with micropolar effective-medium for the cloak (enclosed by white circle). (d) Same as (a) but for a small void with radius $\delta = a/5$, which is adopted for the design of the cloak. (e) – (h) Same as (a) – (d) but for displacement fields, u (horizontal component of the displacements), with an incident longitudinal plane wave.

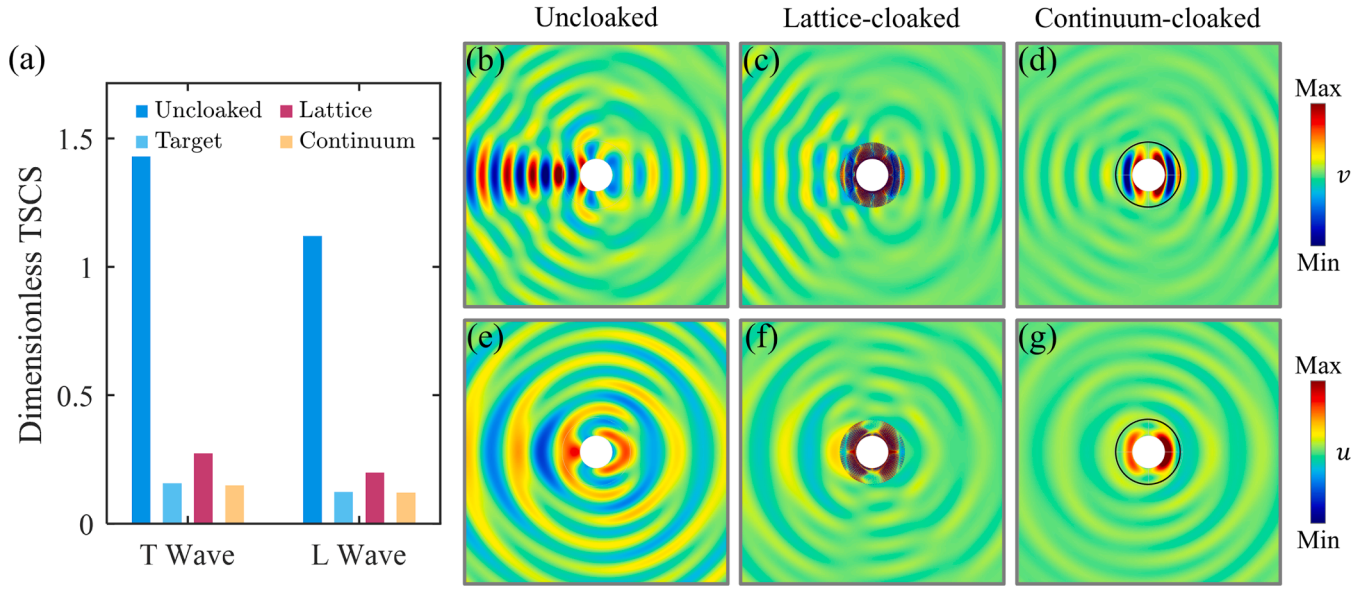

Fig. 8. The TSCS and scattering displacement fields for both the lattice cloak and the continuum cloak. (a) The TSCS for each case is calculated from the scattered displacement fields shown in (b) - (g). The target TSCS is corresponding to the case illustrated in Fig. 7(d) and (h). (b) Simulated scattered displacement fields, v^{sc}, for a transverse plane wave incident onto a void (inner circular white region) with radius a. (c) Same as (b) but with the void covered by the designed microstructure cloak. (d) Same as (c) but with an effective-medium micropolar cloak. (e) - (g) Same as (b) - (d) but for scattered displacement fields, u^{sc}, with an incident longitudinal plane wave.

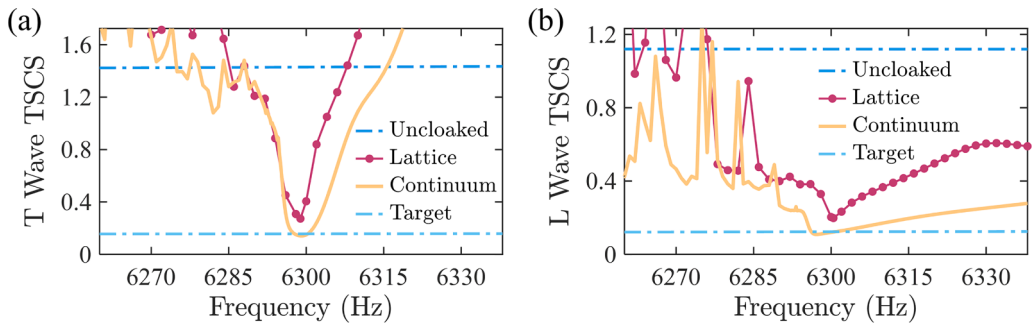

Fig. 9. Frequency dependence of the total scattering cross-section (TSCS) for an uncloaked void, a void covered by a lattice cloak, a void covered by a continuum cloak, and a target small hole under (a) an incident transverse plane wave and (b) an incident longitudinal plane wave.

displacement fields for transverse and longitudinal waves are respectively, $\mathbf{u}^{\text{in}} = \hat{\mathbf{u}}_0 \exp(\mathrm{i}\omega x/c_{\text{T}})$ and $\mathbf{u}^{\text{in}} = \hat{\mathbf{u}}_0 \exp(\mathrm{i}\omega x/c_{\text{L}})$, where c_{T} and c_{L} are corresponding phase velocities in the background media.

By choosing an annular integral path $\partial\Gamma$ enclosing the cloak region, the total scattered power of the cloak can be obtained by integrating over this boundary:

$$E_{\text{sc}} = \oint \frac{1}{2}\mathrm{Re}\left[\sigma_{ij}^{\text{sc}}\dot{\overline{u}}_j^{\text{sc}}\right] n_i ds = -\frac{\omega}{2}\mathrm{Im}\oint n_i \sigma_{ij}^{\text{sc}}\overline{u}_j^{\text{sc}} ds, \tag{28}$$

where $\mathbf{n}$ is the outward normal vector to $\partial\Gamma$, and the overbar denotes the complex conjugate.

The incident power density for a plane wave is given as:

$$P_{\text{in}} = \frac{1}{2}\mathrm{Re}\left[\sigma_{ij}^{\text{in}}\dot{\overline{u}}_j^{\text{in}}\right] n_i = -\frac{\omega}{2}\mathrm{Im}\left[n_i \sigma_{ij}^{\text{in}}\overline{u}_j^{\text{in}}\right], \tag{29}$$

with $\mathbf{n} = (1 \quad 0)^{\text{T}}$. From these, the dimensionless TSCS is computed as $E_{\text{sc}}/(2bP_{\text{in}})$, where b is the radius of the cloak region.

The scattered displacement fields under the excitation of transverse and longitudinal incident waves are shown in Fig. 8. The lattice cloak and the continuum cloak significantly reduces the scattering outside the cloak compared to the unloaded cases in Fig. 8(b) and (e). Quantitatively, the TSCS of the microstructure cloak and the continuum cloak reduces are reduced to one-tenth of the TSCS of a bare rigid scatter, approaching the TSCS of a target void with radius $a/5$. These results clearly validate the efficiency of the designed elastic cloak based on extremal micropolar metamaterials.

We further quantitatively study the TSCS of the continuum and lattice cloaks over a frequency range centered at the operating frequency of 6300 Hz (see Fig. 9). Both the lattice and continuum cloaks significantly suppress scattering at the operating frequency, and the resulting TSCS closely approximates that of the target small hole. However, the performance decreases rapidly beyond a narrow frequency band of nearly 6 Hz. This limitation originates from the dispersive nature of the effective asymmetric elasticity tensor of the micropolar metamaterial (see Eq. (13)), which causes the effective properties to deviate quickly from those required by the transformation method. To achieve broadband performance, one possible strategy is to design large micro-rotation inertia in the metamaterial, which can result in weakly dispersive effective asymmetric elastic properties.

5. Conclusion

Asymmetric elasticity theory and asymmetric elastic materials were conceived to achieve elastic cloaks by using transformation methods nearly two decades ago. The theory shares the same math equations as Cauchy elasticity except that the elasticity tensor only has major symmetry. As a result, the theory can lead to asymmetric stresses, such as by an infinitesimal rotation. However, the asymmetric elasticity theory does not take into account the unbalanced angular momentum caused by the asymmetric stresses. Therefore, the transformation theory based on asymmetric elastic materials still remains controversial today, though elastic cloaks guided by the theory have already been experimentally demonstrated.

Our paper has focused on micropolar elasticity theory, which allows asymmetric stresses and the asymmetric part is balanced by the couple stress and micro-rotation inertia. Specially, we are interested in extremal micropolar materials with zero higher-order elasticity tensor, also termed as reduced Cosserat media. In such media, the micro-rotation DOF can be eliminated from the governing equation for linear momentum. The resulting dynamic equation for displacements becomes the same as the asymmetric elasticity theory, but with an effective dispersive asymmetric elasticity tensor. Therefore, extremal micropolar elastic materials are capable of realizing elastic cloaks based on transformation methods. To verify our finding, we have proposed a metamaterial to realize the extremal micropolar parameters required for cloaking. An elastic cloak has been further designed based on the metamaterial and numerically simulated. The excellent cloaking performance has justified our above finding.

Our finding also indicates that micropolar elasticity theory can provide a rigorous theory for asymmetric elastic materials. This may facilitate the study of other interesting properties in asymmetric elastic materials. Extremal Cauchy materials, e.g., pentamode materials, have shown great potentials in wave control in past few years. Our work also shed light on unusual properties in extremal micropolar materials and may stimulate further exploration.

CRediT authorship contribution statement

Dingxin Sun: Writing – review & editing, Writing – original draft, Methodology, Formal analysis. **Yi Chen:** Writing – review & editing, Writing – original draft, Methodology, Formal analysis, Conceptualization. **Xiaoning Liu:** Writing – review & editing, Writing – original draft, Supervision, Methodology, Formal analysis, Data curation. **Gengkai Hu:** Writing – review & editing, Writing – original draft, Supervision, Project administration, Funding acquisition, Conceptualization.

Declaration of competing interest

The authors declare that they have no known competing financial interests or personal relationships that could have appeared to influence the work reported in this paper.

Acknowledgements

We thank Hongkuan Zhang for valuable discussions. This work is support by the National Natural Science Foundation of China (grant nos 11872017, 11972080, 12532006) and partially by the Alexander von Humboldt foundation.

Appendix A

The mapping gradient is assumed to be diagonal in the principal coordinate, i.e., $\mathbf{F} = F_{11}\mathbf{e}_1\otimes\mathbf{e}_1 + F_{22}\mathbf{e}_2\otimes\mathbf{e}_2 + F_{33}\mathbf{e}_3\otimes\mathbf{e}_3$, with $\mathbf{e}_1$, $\mathbf{e}_2$, and $\mathbf{e}_3$ being the orthonormal bases of the principal coordinate. The required micropolar elastic parameters in the principal coordinate are

$$\rho = \frac{\rho_0}{F_{11}F_{22}F_{33}}, \quad I > 0, \quad A_{ijkl} = 0, \quad D_{ijkl} = 0, \tag{A1}$$

$$\begin{cases} C_{11} = (\lambda_0 + 2\mu_0)\dfrac{F_{11}}{F_{22}F_{33}}, & C_{22} = (\lambda_0 + 2\mu_0)\dfrac{F_{22}}{F_{11}F_{33}}, & C_{33} = (\lambda_0 + 2\mu_0)\dfrac{F_{33}}{F_{11}F_{22}}, \\ C_{12} = \dfrac{\lambda_0}{F_{33}}, & C_{13} = \dfrac{\lambda_0}{F_{22}}, & C_{23} = \dfrac{\lambda_0}{F_{11}}, \\ C_{44} = \dfrac{\mu_0 I\omega^2 F_{22}^2}{\mu_0(F_{22}-F_{33})^2 + I\omega^2 F_{11}F_{22}F_{33}}, & C_{77} = \dfrac{\mu_0 I\omega^2 F_{33}^2}{\mu_0(F_{22}-F_{33})^2 + I\omega^2 F_{11}F_{22}F_{33}}, & C_{47} = \sqrt{C_{44}C_{77}}, \# \\ C_{55} = \dfrac{\mu_0 I\omega^2 F_{11}^2}{\mu_0(F_{11}-F_{33})^2 + I\omega^2 F_{11}F_{22}F_{33}}, & C_{88} = \dfrac{\mu_0 I\omega^2 F_{33}^2}{\mu_0(F_{11}-F_{33})^2 + I\omega^2 F_{11}F_{22}F_{33}}, & C_{58} = \sqrt{C_{55}C_{88}}, \\ C_{66} = \dfrac{\mu_0 I\omega^2 F_{11}^2}{\mu_0(F_{11}-F_{22})^2 + I\omega^2 F_{11}F_{22}F_{33}}, & C_{99} = \dfrac{\mu_0 I\omega^2 F_{22}^2}{\mu_0(F_{11}-F_{22})^2 + I\omega^2 F_{11}F_{22}F_{33}}, & C_{69} = \sqrt{C_{66}C_{99}}. \end{cases} \tag{A2}$$

Data availability

https://dx.doi.org/10.5281/zenodo.17141180 (The data that support the plots within this paper are publically available on the open access data repository of Zenodo [17141180].)

References

[1] Pendry JB, Schurig D, Smith DR. Controlling electromagnetic fields. Science 2006;312:1780.
[2] Milton GW, Briane M, Willis JR. On cloaking for elasticity and physical equations with a transformation invariant form. New J Phys 2006;8:248.
[3] Cummer SA, Schurig D. One path to acoustic cloaking. New J Phys 2007;9:45.
[4] Brun M, Guenneau S, Movchan AB. Achieving control of in-plane elastic waves. Appl Phys Lett 2009;94:61903.
[5] Han T, Bai X, Gao D, Thong JTL, Li B, Qiu C. Experimental demonstration of a bilayer thermal cloak. Phys Rev Lett 2014;112:054302.
[6] Chen Y, Zheng M, Liu X, Bi Y, Sun Z, Xiang P, Yang J, Hu G. Broadband solid cloak for underwater acoustics. Phys Rev B 2017;95:180104.
[7] Schurig D, Mock JJ, Justice BJ, Cummer SA, Pendry JB, Starr AF, Smith DR. Metamaterial electromagnetic cloak at microwave frequencies. Science 2006;314:977.
[8] Chang Z, Hu G. Elastic wave omnidirectional absorbers designed by transformation method. Appl Phys Lett 2012;101:54102.
[9] Chen Y, Liu XN, Hu GK. Latticed pentamode acoustic cloak. Sci Rep 2015;5:15745.
[10] Chang Z, Liu X, Hu G, Hu J. Transformation ray method: controlling high frequency elastic waves (L). J Acoust Soc Am 2012;132:2942.
[11] Colquitt DJ, Brun M, Gei M, Movchan AB, Movchan NV, Jones IS. Transformation elastodynamics and cloaking for flexural waves. J Mech Phys Solids 2014;72:131.
[12] Engheta N, Ziolkowski RW. Metamaterials : physics and engineering explorations. Berlin: Wiley; 2006.
[13] Bertoldi K, Vitelli V, Christensen J, van Hecke M. Flexible mechanical metamaterials. Nat Rev Mater 2017;2:17066.
[14] Kadic M, Milton GW, van Hecke M, Wegener M. 3D metamaterials. Nat Rev Phys 2019;1:198.
[15] Willis JR. Variational principles for dynamic problems for inhomogeneous elastic media. Wave Motion 1981;3:1.
[16] Chen Y, Haberman MR. Controlling displacement fields in polar Willis solids via gauge transformations. Phys Rev Lett 2023;130:147201.
[17] Nassar H, Brucks P. Willis elasticity from microcontinuum field theories: asymptotics, microstructure-property relationships, and cloaking. Wave Motion 2023;122:103206.
[18] Brun M, Guenneau S. Transformation design of in-plane elastic cylindrical cloaks, concentrators and lenses. Wave Motion 2023;119:103124.
[19] Norris AN, Shuvalov AL. Elastic cloaking theory. Wave Motion 2011;48:525.
[20] Yavari A, Golgoon A. Nonlinear and linear elastodynamic transformation cloaking. Arch Ration Mech Anal 2019;234:211.
[21] Ogden RW. Incremental statics and dynamics of pre-stressed elastic materials. Waves in nonlinear pre-stressed materials. Vienna: Springer; 2007. p. 1–26.
[22] Norris AN, Parnell WJ. Hyperelastic cloaking theory: transformation elasticity with pre-stressed solids. Proc R Soc A 2012;468:2881.
[23] Parnell WJ, Norris AN, Shearer T. Employing pre-stress to generate finite cloaks for antiplane elastic waves. Appl Phys Lett 2012;100:171907.
[24] Guo D, Chen Y, Chang Z, Hu G. Longitudinal elastic wave control by pre-deforming semi-linear materials. J Acoust Soc Am 2017;142:1229.
[25] Nassar H, Chen YY, Huang GL. A degenerate polar lattice for cloaking in full two-dimensional elastodynamics and statics. Proc R Soc A 2018;474:20180523.
[26] Nassar H, Chen YY, Huang GL. Isotropic polar solids for conformal transformation elasticity and cloaking. J Mech Phys Solids 2019;129:229.
[27] Nassar H, Chen YY, Huang GL. Polar metamaterials: A new outlook on resonance for cloaking applications. Phys Rev Lett 2020;124:084301.
[28] Xu X, Wang C, Shou W, Du Z, Chen Y, Li B, Matusik W, Hussein N, Huang G. Physical realization of elastic cloaking with a polar material. Phys Rev Lett 2020;124:114301.
[29] Zhang HK, Chen Y, Liu XN, Hu GK. An asymmetric elastic metamaterial model for elastic wave cloaking. J Mech Phys Solid 2020;135:103796.
[30] Zhang Q, Cherkasov AV, Arora N, Hu G, Rudykh S. Magnetic field-induced asymmetric mechanical metamaterials. Extrem Mech Lett 2023;59:101957.
[31] Zhang Q, Hu G, Rudykh S. Magnetoactive asymmetric mechanical metamaterial for tunable elastic cloaking. Int J Solid Struct 2024;289:112648.
[32] Ramakrishna SAnantha. Physics of negative refractive index materials. Rep Prog Phys 2005;68:449.
[33] Chen Y, Kadic M, Wegener M. Roton-like acoustical dispersion relations in 3D metamaterials. Nat Commun, 2021;12:3278.
[34] Milton GW, Cherkaev AV. Which elasticity tensors are realizable? J Eng Mater Technol 1995;117:483.
[35] Kadic M, Bückmann T, Stenger N, Thiel M, Wegener M. On the practicability of pentamode mechanical metamaterials. Appl Phys Lett 2012;100:191901.
[36] Kadic M, Bückmann T, Schittny R, Wegener M. On anisotropic versions of three-dimensional pentamode metamaterials. New J Phys 2013;15:023029.
[37] Chen Y, Liu X, Xiang P, Hu G. Pentamode material for underwater acoustic wave control. Adv Mech 2016;46.
[38] Fraternali F, Amendola A. Mechanical modeling of innovative metamaterials alternating pentamode lattices and confinement plates. J Mech Phys Solid 2017;99:259.
[39] Sun Z, Jia H, Chen Y, Wang Z, Yang J. Design of an underwater acoustic bend by pentamode metafluid. J Acoust Soc Am 2018:143.
[40] Sun Z, Sun X, Jia H, Bi Y, Yang J. Quasi-isotropic underwater acoustic carpet cloak based on latticed pentamode metafluid. Appl Phys Lett 2019;114:94101.
[41] Dong H, Zhao S, Miao X, Shen C, Zhang X, Zhao Z, Zhang C, Wang Y, Cheng L. Customized broadband pentamode metamaterials by topology optimization. J Mech Phys Solids 2021;152:104407.
[42] Norris AN. Acoustic cloaking theory. Proc R Soc A 2008;464:2411.
[43] Chen Y, Liu X, Hu G. Influences of imperfectness and inner constraints on an acoustic cloak with unideal pentamode materials. J Sound Vib 2019;458:62.
[44] Milton GW. Complete characterization of the macroscopic deformations of periodic unimode metamaterials of rigid bars and pivots. J Mech Phys Solid 2013;61:1543.

[45] Chen Y, Hu G. Broadband and high-transmission metasurface for converting underwater cylindrical waves to plane waves. Phys Rev Appl 2019;12:044046.
[46] Deng B, Li J, Tournat V, Purohit PK, Bertoldi K. Dynamics of mechanical metamaterials: A framework to connect phonons, nonlinear periodic waves and solitons. J Mech Phys Solid 2021;147:104233.
[47] Groß MF, Schneider JLG, Wei Y, Chen Y, Kalt S, Kadic M, Liu X, Hu G, Wegener M. Tetramode metamaterials as phonon polarizers. Adv Mater 2023;35:2211801.
[48] Zhang Q, Cherkasov AV, Xie C, Arora N, Rudykh S. Nonlinear elastic vector solitons in hard-magnetic soft mechanical metamaterials. Int J Solid Struct 2023;280:112396.
[49] Groß MF, Schneider JLG, Chen Y, Kadic M, Wegener M. Dispersion engineering by hybridizing the back-folded soft mode of monomode elastic metamaterials with stiff acoustic modes. Adv Mater 2024;36:2307553.
[50] Auffray N, Le Quang H, He QC. Matrix representations for 3D strain-gradient elasticity. J Mech Phys Solid 2013;61:1202.
[51] Eringen AC. Microcontinuum field theories : I. foundations and solids. New York: Springer; 1999.
[52] Chen Y, Liu X, Hu G, Sun Q, Zheng Q. Micropolar continuum modelling of bi-dimensional tetrachiral lattices. Proc R Soc A 2014;470:20130734.
[53] Duan S, Wen W, Fang D. A predictive micropolar continuum model for a novel three-dimensional chiral lattice with size effect and tension-twist coupling behavior. J Mech Phys Solid 2018;121:23.
[54] Pal'mov VA. Fundamental equations of the theory of asymmetric elasticity. J Appl Math Mech 1964;28:496.
[55] Arslan H, Sture S. Finite element simulation of localization in granular materials by micropolar continuum approach. Comput Geotech 2008;35:548.
[56] Khlopotin A, Olsson P, Larsson F. Transformational cloaking from seismic surface waves by micropolar metamaterials with finite couple stiffness. Wave Motion 2015;58:53.
[57] Abreu R, Kamm J, Reiß A-S. Micropolar modelling of rotational waves in seismology. Geophys J Int 2017;210:1021.
[58] Prakash V, Behera AK, Rahaman MM, Roy D. A micropolar phase field model for inner-structure sensitive quasi-brittle failure. Int J Mech Sci 2025;303:110615.
[59] Behera AK, Unnikrishna Pillai A, Das A, Rahaman MM. A micropolar phase-field model for size-dependent electro-mechanical fracture. Int J Mech Sci 2025;285:109805.
[60] Kulesh M, Grekova E, Shardakov I. The problem of surface wave propagation in a reduced Cosserat medium. Acoust Phys 2009;55:218.
[61] Grekova E. Linear reduced cosserat medium with spherical tensor of inertia, where rotations are not observed in experiment. Mech Solid 2012;47:538.
[62] Li P, Hou X, Yang F, Wang P, Zhao J, Fan H. Symmetric elastic wave cloak design for underground protective structures based on multi-center coordinate transformation. Acta Mech 2024;235:2761.
[63] Chatzopoulos Z, Palermo A, Diatta A, Guenneau S, Marzani A. Cloaking Rayleigh waves via symmetrized elastic tensors. Int J Eng Sci 2023;191:103899.
[64] Fielding SM. Simple and effective mechanical cloaking. J Mech Phys Solid 2024;192:105824.
[65] Sozio F, Shojaei MF, Yavari A. Optimal elastostatic cloaks. J Mech Phys Solid 2023;176:105306.
[66] Cheng X, Liu C, Zhang W, Tang Z, Liu Y, Tang S, Du Z, Cui T, Guo X. A compatible boundary condition-based topology optimization paradigm for static mechanical cloak design. Extrem Mech Lett 2023;65:102100.
[67] Goda I, Assidi M, Belouettar S, Ganghoffer JF. A micropolar anisotropic constitutive model of cancellous bone from discrete homogenization. J Mech Behav Biomed Mater 2012;16:87.
[68] Colatosti M, Carboni B, Fantuzzi N, Trovalusci P. Composite material identification as micropolar continua via an optimization approach. Compos, Part C: Open Access 2023;11:100362.
[69] Bacigalupo A, De Bellis ML, Zavarise G. Asymptotic homogenization approach for anisotropic micropolar modeling of periodic Cauchy materials. Comput Method Appl Mech Eng 2022;388:114201.
[70] Huang L, Yuan H, Zhao H. An FEM-based homogenization method for orthogonal lattice metamaterials within micropolar elasticity. Int J Mech Sci 2023;238:107836.
[71] Guo Z, Liu X, Huang L, Adhikari S, Liang X. Analytical homogenization for equivalent in-plane elastic moduli of prestressed lattices based on the micropolar elasticity model. Compos Struct 2024;346:118391.
[72] He LH, Shen CY. Micropolar modeling for bending shape of 2D lattices: the case of equilateral triangular cell structure. Extrem Mech Lett 2025;74:102281.
[73] Lemkalli B, Kadic M, El Badri Y, Guenneau S, Bouzid A, Achaoui Y. Mapping of elastic properties of twisting metamaterials onto micropolar continuum using static calculations. Int J Mech Sci 2023;254:108411.
[74] Gad AI, Gao XL, Li K. A strain energy-based homogenization method for 2-D and 3-D cellular materials using the micropolar elasticity theory. Compos Struct 2021;265:113594.
[75] Liu XN, Huang GL, Hu GK. Chiral effect in plane isotropic micropolar elasticity and its application to chiral lattices. J Mech Phys Solid 2012;60:1907.
[76] Bacigalupo A, Gambarotta L. Generalized micropolar continualization of 1D beam lattices. Int J Mech Sci 2019;155:554.
[77] Bacigalupo A, Gambarotta L. Identification of non-local continua for lattice-like materials. Int J Eng Sci 2021;159:103430.
[78] Diana V, Bacigalupo A, Gambarotta L. Thermodinamically-consistent dynamic continualization of block-lattice materials. Int J Solid Struct 2023;262-263:112050.
[79] Bacigalupo A, Badino P, Diana V, Gambarotta L. Enhanced high-frequency continualization scheme for inertial beam-lattice metamaterials. Int J Mech Sci 2025;286:109794.
[80] Cheikho K, Laurent C, Ganghoffer JF. An advanced method to design graded cylindrical scaffolds with versatile effective cross-sectional mechanical properties. J Mech Behav Biomed Mater 2022;125:104887.
[81] Cheikho K, Ganghoffer JF, Baldit A, Labbé E, Alix S, Kerdjoudj H, Mauprivez C, Lebée A, Laurent C. A flexible design framework to design graded porous bone scaffolds with adjustable anisotropic properties. J Mech Behav Biomed Mater 2023;140:105727.
[82] Alavi SE, Cheikho K, Laurent C, Ganghoffer JF. Homogenization of quasi-periodic conformal architectured materials and applications to chiral lattices. Mech Mater 2024;199:105146.
[83] Chen Y, Liu X, Hua G. Design of arbitrary shaped pentamode acoustic cloak based on quasi-symmetric mapping gradient algorithm. J Acoust Soc Am 2016;140:EL405.
[84] Chen Y, Frenzel T, Guenneau S, Kadic M, Wegener M. Mapping acoustical activity in 3D chiral mechanical metamaterials onto micropolar continuum elasticity. J Mech Phys Solid 2020;137:103877.
[85] Lakes RS, Benedict RL. Noncentrosymmetry in micropolar elasticity. Int J Eng Sci 1982;20:1161.
[86] Bacigalupo A, Gambarotta L. Wave propagation in non-centrosymmetric beam-lattices with lumped masses: discrete and micropolar modeling. Int J Solid Struct 2017;118:128.
[87] Kishine J, Ovchinnikov A, Tereshchenko A. Chirality-induced phonon dispersion in a noncentrosymmetric micropolar crystal. Phys Rev Lett 2020;125:245302.
[88] Chen Y, Schneider JLG, Groß MF, Wang K, Kalt S, Scott P, Kadic M, Wegener M. Observation of chirality-induced roton-like dispersion in a 3D micropolar elastic metamaterial. Adv Funct Mater 2023;34.
[89] Giorgio I, dell'Isola F, Misra A. Chirality in 2D cosserat media related to stretch-micro-rotation coupling with links to granular micromechanics. Int J Solid Struct 2020;202:28.
[90] Cui Z, Ju J. Mechanical coupling effects of 2D lattices uncovered by decoupled micropolar elasticity tensor and symmetry operation. J Mech Phys Solid 2022;167:105012.
[91] Auffray N, El Ouafa S, Rosi G, Desmorat B. Anisotropic structure of two-dimensional linear cosserat elasticity. Math Mech Compl Sys 2022;10:321.
[92] Chen Y. Postdoctoral research report: study of acoustic/elastic wave control with metamaterials. Beijing: Beijing Institute of Technology; 2020.
[93] Kittel C. Introduction to solid state physics. New York: Wiley; 2005.
[94] Lu J, Qiu C, Xu S, Ye Y, Ke M, Liu Z. Dirac cones in two-dimensional artificial crystals for classical waves. Phys Rev B 2014;89:134302.